

Strength and failure of an aluminum/PA66 self-piercing riveted assembly at low and moderate loading rates: Experiments and modeling

Nicolas Leconte, Benjamin Bourel, Franck Lauro, Claudiu Badulescu, Eric Markiewicz

▶ **To cite this version:**

Nicolas Leconte, Benjamin Bourel, Franck Lauro, Claudiu Badulescu, Eric Markiewicz. Strength and failure of an aluminum/PA66 self-piercing riveted assembly at low and moderate loading rates: Experiments and modeling. International Journal of Impact Engineering, 2020, 142, pp.103587-1 - 103587-23. 10.1016/j.ijimpeng.2020.103587 . hal-02638901

HAL Id: hal-02638901
https://hal.science/hal-02638901

Submitted on 23 Mar 2022

HAL is a multi-disciplinary open access archive for the deposit and dissemination of scientific research documents, whether they are published or not. The documents may come from teaching and research institutions in France or abroad, or from public or private research centers.

L'archive ouverte pluridisciplinaire **HAL**, est destinée au dépôt et à la diffusion de documents scientifiques de niveau recherche, publiés ou non, émanant des établissements d'enseignement et de recherche français ou étrangers, des laboratoires publics ou privés.

Strength and failure of an aluminum/PA66 self-piercing riveted assembly at low and moderate loading rates: Experiments and modeling

N. Leconte[a,*], B. Bourel[a], F. Lauro[a], C. Badulescu[b], E. Markiewicz[a]

[a] Univ. Polytechnique Hauts-de-France, CNRS, UMR 8201 - LAMIH, Valenciennes F-59313, France
[b] ENSTA Bretagne, IRDL, UMR CNRS 6027, 29806 Brest Cedex 9, France

The self piercing riveting (SPR) process is increasingly used in the automotive industry due to its ability to connect multi-materials for weight reduction considerations. The strength and failure of such multi-material assemblies need to be characterized and modelled for full-scale structural computations. An aluminum/PA66 composite 2-sheet SPR assembly is characterized in pure and mixed tensile/shear single connection Arcan ex-periments. The peak force and dissipated energy increase with the loading angle. Neither loading velocity sensitivity in the range $0.016mm/s$ $100mm/s$ nor Pa66 composite fiber orientation sensitivity are observed. Some failure modes of aluminum-aluminum SPR are observed. Experiments are also carried out on a single hat component with multiple connections for two loading rates: 5mm/s and 1500 mm/s. The maximum forces and dissipated energies slightly increase at 1500mm/s. Both tensile and shear dominated mode mix ratio values are experienced by the connections. A 13 independent parameter SPR connector model is employed to model the metallic-composite SPR joint. It features three b-norm criteria employed for irreversible deformation, maximum force and failure. It can be generated by combining some elementary behaviors of the general connector model of Abaqus. The calibration procedure decouples the pure tensile/shear contributions from the mixed tensile/shear ones. The parameters are identified based on the Arcan tests and validated on the component experiments. The overall comparison between computations and experiments show satisfactory results.

1. Introduction

The self-piercing riveting (SPR) has been increasingly adopted by many industries as a high-speed mechanical fastening technique for the joining of sheet material. Although this process is a young joining technology, it has become more and more popular during the last decade, especially in the automotive industry where multi-material assembly has become a priority. The main interest comes from its capability to join a wide range of similar or dissimilar materials without the need for a pre-drilled hole. This single-step fastening technique is quick and inexpensive. The semi-tubular rivet is directly pushed into the sheets to clamp together thanks to a press tool with a blank holder and a die. Other advantages, like the low sensitivity to corrosion in comparison with the spot welded joints, are a great motivation for the use of the SPR joints in automotive industry, especially for crash-worthiness applications. Additionally, it may be combined with other techniques, like adhesive bonding, in order to create hybrid joints.

The performance of joints needs to be studied so as to employ them in the design of transportation structures. Experiments can be conducted to characterize their static [1], fatigue [2], and fast dynamics performance [3], while numerical models are required to perform quick evaluations and to reduce the costs.

A quite complete overview of the topics linked to the characterization and modeling of riveted assemblies is provided by Langrand et al. [4]. Indeed, the topics addressed in the particular case of a countersunk riveted assembly joining aluminum plates include:

- the characterization and modeling of the riveting process,
- the analysis of the influence of the residual stress state due to the process on the assembly's strength and failure,
- the quasi-static and fast dynamics characterization of the assembly's strength and failure based on single lap, cross tensile, Arcan pure and mixed tensile/shear, and aircraft component experiments,
- the detailed FE modeling of the assembly's strength where plasticity and damage model parameters are identified by an inverse approach,
- the linking of process and strength assembly fine models,
- the comparison and proposal of equivalent models dedicated to

* Corresponding author.
E-mail address: nicolas.leconte@uphf.fr (N. Leconte).

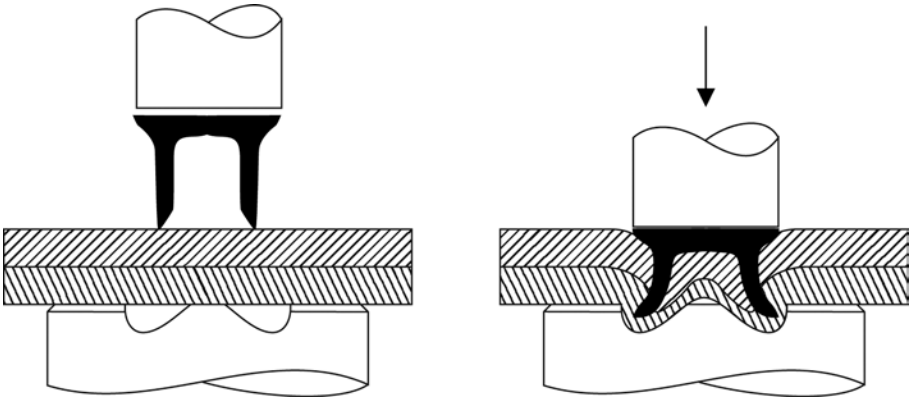


Fig. 1. Joining process of the self-piercing rivet connection.

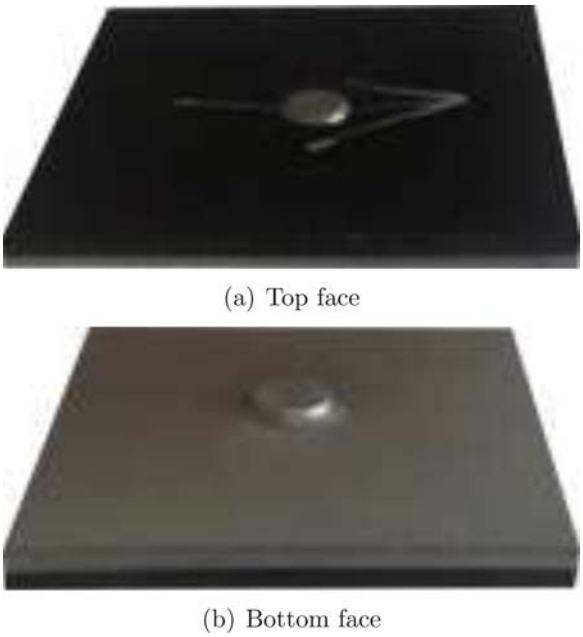


Fig. 2. SPR specimen made of aluminum and Pa66.

Table 1
Pa66 properties.

Pa66 HF consolidated	
Morphology	5 layers, 8H Satin balanced
Fibers content	50% (Glass fiber)
Sheet Thickness	$2mm$
Density	$1.47t/m^3$
Elastic modulus (0°)	$27GPa$
Elastic modulus (90°)	$27GPa$
Shear modulus	$2.6GPa$
Poisson ratio	0.25

Table 2
Aluminum 5182 properties.

Aluminium 5182	
Chemical composition	4.74% Mg, 0.38% Mn, 0.25% Fe, 0.10% Si
Sheet Thickness	$2mm$
Density	$2.7t/m^3$
Ultimate strength	$400MPa$
Yield strength (0.2%)	$147MPa$
Elastic modulus	$75GPa$
Poisson ratio	0.33
Elongation at failure	25%

structural computations.

The experiments on SPR assemblies can be sorted by considering mainly the nature of the sheets joined and their number, the nature of the rivet, the type of loading or specimen, the rate of loading, and the number of connections involved.

The quasi-static strength and failure of SPR assemblies in which two similar or dissimilar metallic sheets are joined is quite extensively studied [1,3,5–12]. Aluminum - aluminum [1,3,6–8,10], steel - steel [9,11,12], and steel - aluminum assemblies were studied [3,5]. Han et al. [13] have studied the strength of 3 sheet metallic SPR assemblies and Hoang et al. studied the material of the metallic rivet [7]. Porcaro et al. [1] have extensively studied the quasi-static behavior and failure of self-piercing riveted (SPR) connections between aluminum plates. The influence of the aluminum plate tempers and thicknesses were also studied. It resulted in particular in the classification of the failure modes related to mixed tensile/shear and peeling loadings.

Porcaro et al. [10] have studied the fast dynamics behavior of single lap and pull out aluminum SPR assemblies using Kolsky Hopkinson bars. No obvious dependency of the maximum forces and failure modes to the loading velocity was observed. Sun and Khaleel [3] used a servo-hydraulic system to study the strength of similar and dissimilar aluminum/steel single lap coach peel and cross tension SPR assemblies. They concluded however that SPR joint strength increases when increasing the loading rate.

Some authors characterized the connection using single connection tests such as cross tensile [3,6,12], single lap [1,3,5,6,9,11,13], coach peel [1,3,6,7,9,13], mixed tensile-shear Arcan-type experiments [1,6–8], and some used multi connection component experiments [6,7]. For both single connection and multi connection experiments, the response of the assembly should not be “hidden” by predominant sheet response, i.e. the connection should contribute significantly to the global force displacement response.

It is finally worth noting that point-to-point assemblies in which at least one laminate is joined have not that much been characterized. Single lap quasi static and fatigue tests were performed by Ueda et al. [14] on 2-sheet carbon fiber reinforced laminate SPR assemblies. Kapi et al. [15] have characterized aluminum - carbon fiber reinforced polymer sheets joined by a titanium bolt in single lap experiments.

The numerical models of point-to-point assemblies can be sorted in two categories: the finely meshed and geometrically accurate meso-scale models on the one hand [1,4,8,10,15–17], and the macro-scale models dedicated to structural computations on the other hand [4,18–27]. The meso-scale models can either be dedicated to the assembly process [1,4,8,16] or to the assembly’s strength and failure [1,4,8,17], while macro models deal with the assembly’s strength and failure only.

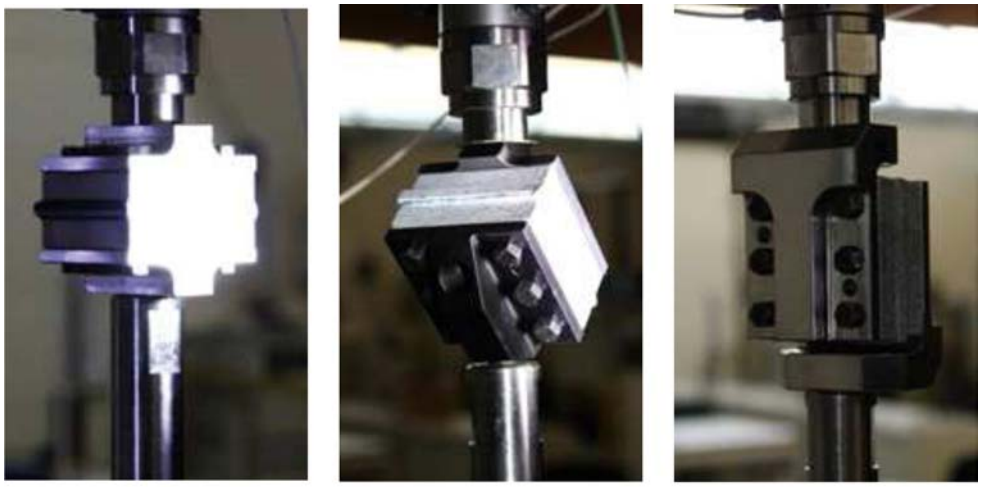


Fig. 3. Experimental setup of the modified dynamic Arcan test.

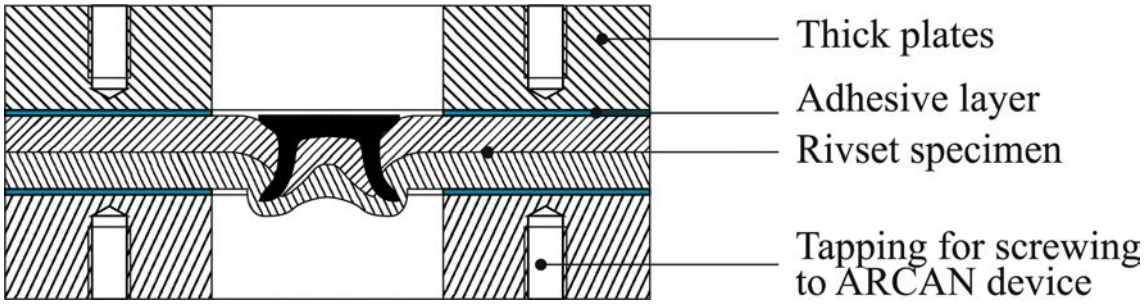


Fig. 4. SPR specimen design for dynamic Arcan test.

A macro model is an abstraction that is designed to be as much as possible able to model the complex phenomena occurring in the assembly without having to model it finely (geometry, contact, material behavior, etc.) to be less expensive than meso-scale models in structural computations. Many models can be found in the literature. Some models are based on constraints or rigid elements that can be assembled in a generic pattern [28–30]. With this approach, it seems possible to find a pattern that makes the macro model of the assembly results fit the experimental ones. However, it becomes more difficult to obtain this agreement for many loading kinds. Moreover, it seems also difficult to obtain a generic recipe to decide the a priori suitable rigid element pattern. Other approaches employ connector elements. Generally a single element is employed to model the connection. The element can be of spring or beam nature and includes complex behaviors (elasticity, plasticity, damage, etc.) that allow representing many point-to-point assemblies responses. Langrand et al. proposed a model for riveted joints [4], Combescure et al. [18], Langrand et al. [19], and Chtourou et al. [25] proposed models for 2-sheet spot-welded assemblies, Chtourou et al. [21] proposed a model for 3-sheet spot-welded assemblies, Weyer et al. [23], and Hanssen et al. [20] provided models for SPR joints, Berot et al. [24] for bolted joints, and Breda et al. studied decoupled elastic / coupled plastic and decoupled elastic / decoupled plastic models to describe the strength of clinched joints [22]. Bier et al. evaluated an elastic perfectly plastic model with linear damage featuring a single criterion for SPR joints. They modified this model including three criteria, weighting parameters and a load symmetry factor in order to obtain a better agreement between experiments and computations in peeling tests [31,32]. Wang et al. also used the same model for aeronautical riveted joints [27]. These approaches showed that it was possible to obtain satisfactory results for different loading kinds (tensile, shear, mixed tensile/shear, bending) and specimens (single connection specimens, multiple connection components) with a single set of parameters often obtained by calibration or using an inverse approach.

However, to the knowledge of the authors, no macroscopic model dedicated to metallic-composite SPR connections can be found in the open literature. Moreover, experiments were neither conducted until now to characterize the mixed tensile/shear strength and failure of metallic-composite SPR joints, nor to characterize the strength and failure of such components. It is thus proposed to characterize the aluminum-PA66 SPR joint using macroscopic loading speeds that lead to low and moderate strain rates at a local level, and to provide a macroscopic model of this joint.

The article is organized as follows. Section 2 presents Arcan experiments on aluminum-PA66 single connection riveted specimens. A SPR connection formulation and the corresponding parameter calibration procedure are then presented in Section 3 to model the Arcan experiments. Component experiments are presented and modelled in Section 4. Finally, some conclusions are drawn in Section 5.

2. Arcan experiments

In this section, the Arcan single connection experiments are presented. The SPR assembly is presented first. Then the experimental procedure is described. Finally the experimental results are analyzed.

2.1. Aluminum / PA66 composite SPR assembly

The assembly to be characterized is made of two 2mm thick 50mm x 50mm sheets. The self-piercing riveting process consists in pushing the

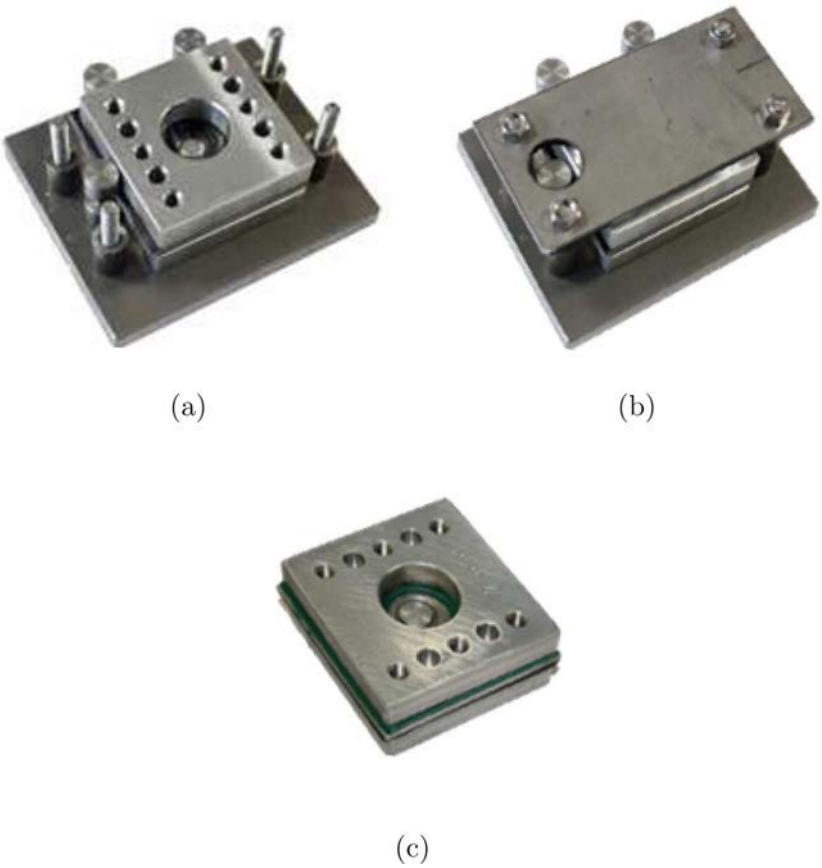


Fig. 5. Fixture system of the SPR specimens during the adhesive curing.

rivet through these two sheets. The rivet made of high-strength steel penetrates into the top plate, and the die shape causes the rivet to flare within the lower sheet in order to form a mechanical interlock (Fig. 1). In this work, these assemblies were made by Bollhoff company on metallic / composite sheets (Fig. 2). A PA66 composite, constitutes the perforated part (top plate) of the assembly. PA66 is a long glass fiber reinforced nylon 6/6 (polyamide 6/6) thermoplastic composite. It is made using a 8H satin weave. An aluminum 5182-O alloy sheet constitutes the flared part (bottom plate) of the assembly. The mechanical properties of these two base materials are given in Tables 1 and 2.

2.2. Dynamic Arcan test

An experimental device has been designed to load SPR joints in pure tensile, pure shear, and mixed tensile/shear modes (Fig. 3). The design is based on a modified Arcan fixture developed for dynamic loads [21,33]. The low mass of this device allows lowering noise in the dynamic response. It allows to reach high loading speeds (up to 100*mm/s*), while preventing the measured force to be disturbed by device inertia effect, i.e. wave propagation effects and load cell ringing effects. A dedicated device is used for each of the three loading angles: pure tensile (0°), mixed tensile/shear (45°), and pure shear (90°).

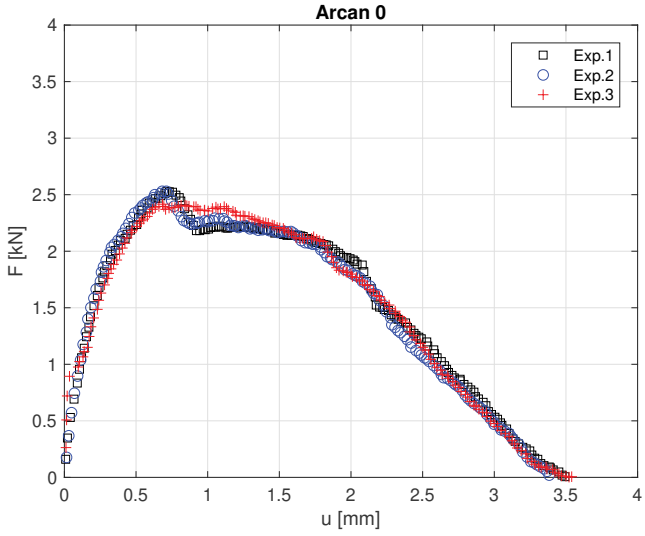
The assembly to be characterized is placed at the center of the device. It is fixed to the upper and lower parts of the Arcan device by means of two aluminum thick plates. These plates are drilled (diameter 20mm) in order to release the central area of the assembly located around the SPR. The assembly is fixed on the thick plates by bonding (Fig. 4). The adhesive used is a single-component epoxy adhesive (Betamate 1822).

The bonded surface has been defined to ensure that the adhesive only experiences elastic strain during the test. Consequently, the fracture always occurs in the SPR joint and not in the adhesive joint. The adhesive curing is carried out by means of a special fixture device. It ensures the good centering of the two thick plates on the rivet axis, but also a uniform thickness of the adhesive (0.3mm) during the polymerization (Fig. 5). The small thickness of the adhesive layer permits to neglect the deformation of the glue when compared to the deformation of the riveted assembly.

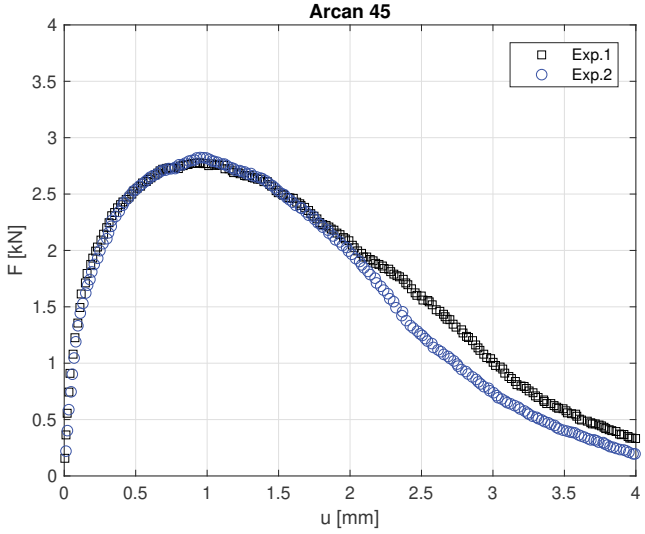
The complete block, composed of the SPR assembly bonded to two aluminum thick plates is then tight to the upper and lower parts of the Arcan device using 6 screws. The whole block is finally installed on the dynamic machine. The upper part is attached to the fixed crossbar of the machine, and the lower part on the movable rod of the jack. All the specimens were loaded by means of a fast hydraulic jack of capacity 65kN. The loading is done on a range of the jack displacement ensuring a good control of the imposed speed. A slider system ensures a uniform speed of the piston during the tests. A uniaxial piezoelectric cell (KESTLER 30KN) mounted on the crosshead of the machine ensures the effort measurement. This cell is connected to a YOKOGAWA DL750 acquisition system. The relative displacement between the lower and upper plates of the assembly is measured by digital image correlation (DIC) [34] by means of VIC 2D Software. The images are obtained by a Photron APX RS 3000 dynamic camera. The thick plates are assumed rigid in comparison with the global assembly stiffness so as to neglect their deformation. Then, the opening (in tension) and the sliding (in shear) of the assembly are directly obtained by the relative displacement between the two plates. A speckle pattern was applied on the thick plate flank by using a standard white and black spray paint. The displacement is measured at several points taken along a line parallel to the assembly plane, so as to calculate an average displacement for each of the two parts.

2.3. Experimental results and failure modes

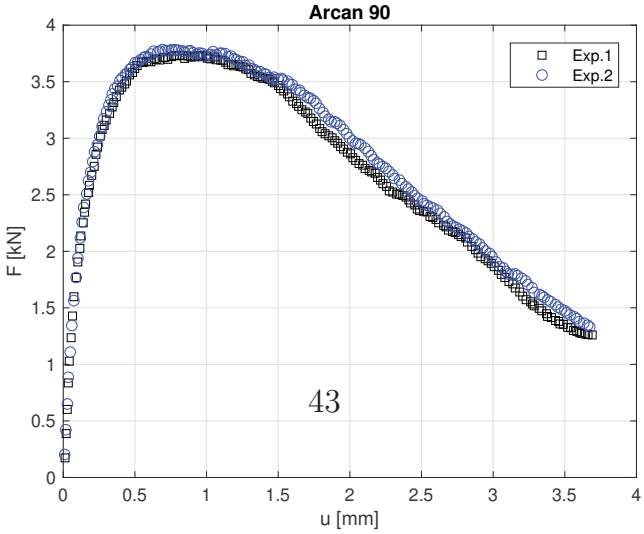
Fig. 6 shows the global force-displacement responses observed for



(a) Pure tensile



(b) Tensile/shear



(c) Pure shear

Fig. 6. Force-displacement curves for Arcan tests.

Table 3
Comparison of Arcan maximum forces.

	0°	45°	90°
Test 1 (kN)	2.53	2.78	3.73
Test 2 (kN)	2.53	2.82	3.78
Test 3 (kN)	2.42	–	–
Mean (kN)	2.49	2.80	3.76
Coefficient of mean deviation (%)	2.03	0.82	0.66

Table 4
Comparison of Arcan dissipated energies.

	0°	45°	90°
Test 1 (J)	5.39	7.12	9.95
Test 2 (J)	5.31	6.59	10.25
Test 3 (J)	5.35	–	–
Mean (J)	5.35	6.85	10.10
Coefficient of mean deviation (%)	0.46	3.83	1.50

Table 5
Comparison of Arcan displacements at maximum force.

	0°	45°	90°
Test 1 (mm)	0.71	0.95	0.81
Test 2 (mm)	0.68	0.95	0.69
Test 3 (mm)	0.68	–	–
Mean (mm)	0.69	0.95	0.75
Coefficient of mean deviation (%)	1.99	0.24	7.87

the assembly for each of the three loading angles for a loading speed of $1mm/s$: pure tensile (0°), mixed tensile/shear (45°) and pure shear (90°). Note that these curves are quite similar to those observed in aluminum-aluminum SPR assembly tests [1]. A good repeatability of the tests is observed. The proposed device shows a good efficiency leading to very low dispersions on the force-displacement response, and this regardless of the loading angle. The dispersion can be evaluated using the coefficient of mean deviation (CMD) applied to a generic quantity x:

$$CMD(x) = \frac{1}{n}\sum_{i}^{n}\left|\frac{x(i)-\bar{x}}{\bar{x}}\right| * 100 \tag{1}$$

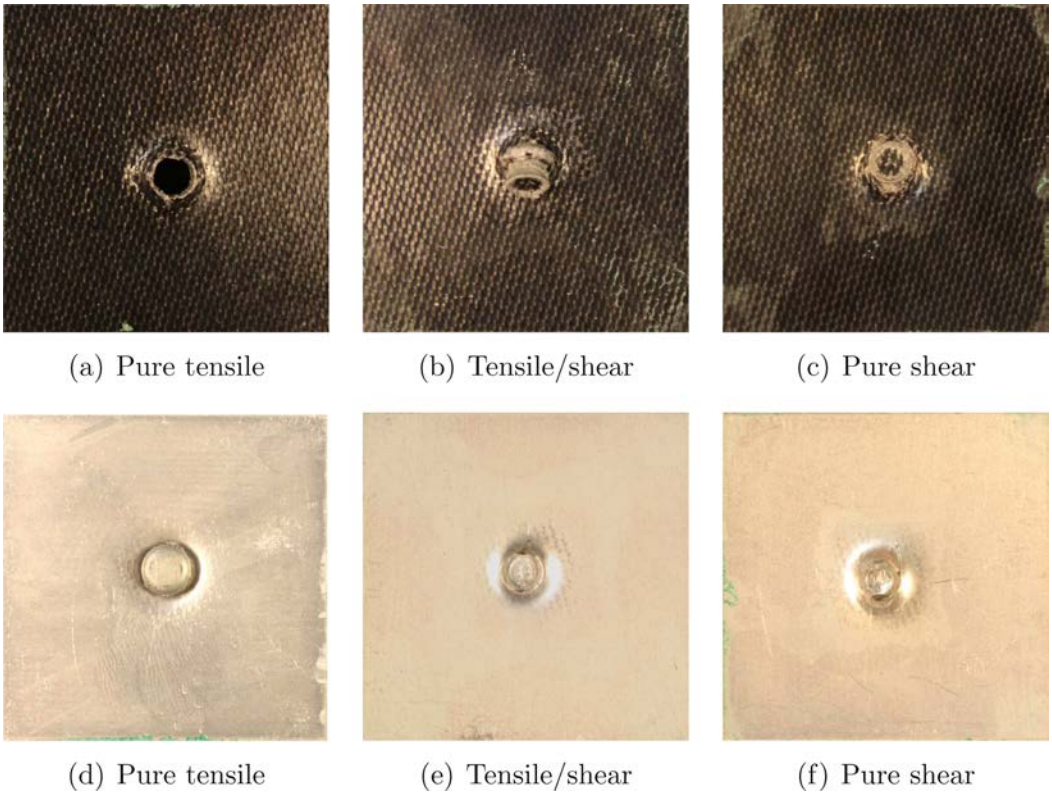


Fig. 7. Failure modes of the SPR assemblies in pure tensile, mixed tensile/shear and pure shear loadings.

where i corresponds to a sample, n to the number of samples, and $\bar{x}$ to the average of x. This coefficient in used in the various tables of this paper

The mechanical behavior of the SPR assembly can be divided into several phases depending on the angle considered. The first one corresponds to the increase of the effort until a peak force is reached. More precisely, a quasi-linear response is observed at first. Then it becomes more and more non-linear until the peak force is reached. At 0° and 90°, the post peak phase corresponds to a slowly decreasing force plateau. It is then followed by a quicker force decrease in the last phase, which is quite linear. Note that at 0° two of the three responses exhibit a small post-peak force drop followed by a plateau, while this force drop is absent from the third one. In the mixed tensile-shear case (45°), no force plateau is observed after the maximum force, and the force decrease phase is quicker and not that linear.

The maximum load (Table 3) as well as the initial stiffness increased when increasing the loading angle. The same behavior is observed in aluminum-aluminum SPR assembly tests [1]. Also, the displacement at failure tends to be monotonous with the loading angle (considering extrapolation of the 90° results). Finally the dissipated energy also increases with the loading angle (Table 4). However, contrarily to metallic SPR assemblies, no obvious monotonous tendency between the displacement at maximum force and the loading angle appeared (Table 5). Indeed, the displacement at maximum force at 0° and 90° is inferior to that observed at 45°. This is different to what was observed in aluminum-aluminum SPR assembly tests, where the displacement at failure decreased with the loading angle [1].

Whatever the loading angle considered, the rivet remained elastic in the tests. The failure modes observed were either a pull-out of the rivet on the aluminum sheet side (Fig. 7) in the pure shear and mixed tensile shear tests or an unbuttoning with a rivet going out from the top plate in the pure tensile tests. In the case of the pure shear loading, after unbuttoning, the rivet slips between the two substrates, causing a transverse opening of the specimen (Fig. 8). This mechanism has already been observed in aluminum-aluminum SPR assemblies [10]. Note that the pure shear experiments had to be interrupted after having significantly overtaken the peak force in order to prevent the excessive opening from damaging the cylinder rod. Consequently, the corresponding curves are also interrupted (Fig. 6).

The failure modes also appear to be in connection with that of aluminum-aluminum SPR assemblies. Indeed, Porcaro et al. have identified five failure modes for pure and mixed tensile shear aluminum-aluminum SPR assemblies [1]. Among these modes, two are defined as follows:

Failure mode Fs1 : Shear failure mode. Tilting and pull-out of the rivet from the bottom plate. The rivet rotated generating yield and fracture in the material of the top plate while it is sliding out from the bottom plate.

Failure mode Fs5 : Tensile failure mode. Pull-over of the sheeting. The rivet goes out from the top plate dragging the material under the rivet head.

According to these definitions, the failure modes of the aluminum-PA66 SPR assembly can be labeled *Fs*5 for pure tensile, *Fs*1 for pure shear, and *Fs*1 for mixed tensile/shear. Note that the three other identified failure modes for aluminum-aluminum SPR assemblies have not appeared in the experiments for the aluminum-PA66 SPR assembly.

In order to evaluate the load speed sensitivity, the results were compared to a series of similar tests conducted by ENSTA Bretagne in quasi-static conditions (0.016*mm/s*, Fig. 10). The three loading angles were tested at this loading speed. Fig. 10 shows the failure envelopes obtained from the normal (FN) and shear components (FS) of the maximum forces measured on each test. Based on this comparison, it is not possible to conclude about a significant load speed sensitivity of the assembly's strength in this loading speed range. The results at 1*mm/s* were also compared to a series of similar tests conducted at 100*mm/s* for a pure tensile loading (Fig. 11). The main differences rely in the absence of post-peak small force drop and in a higher displacement at peak force in the 100*mm/s* experiments. The shape of the curves is

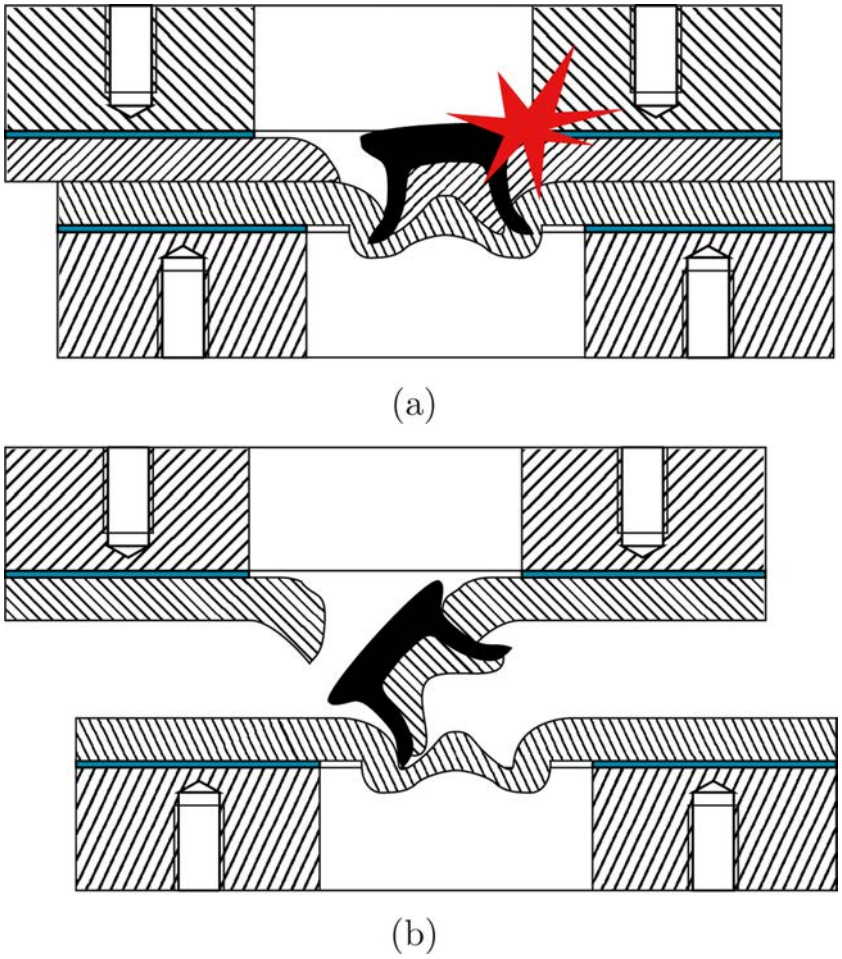


Fig. 8. Unbuttoning mechanism for shear load.

Table 6
Pure tensile features at 100*mm/s*.

	Peak force (kN)	Displacement at peak force (mm)	Energy (J)
Test 1	2.50	0.49	5.35
Test 2	2.52	1.57	6.27
Test 3	2.25	1.75	5.24
Mean	2.42	1.27	5.62
Coefficient of mean deviation (%)	4.68	40.81	7.67

Table 7
45° mixed tensile shear tests with 90° fiber orientation.

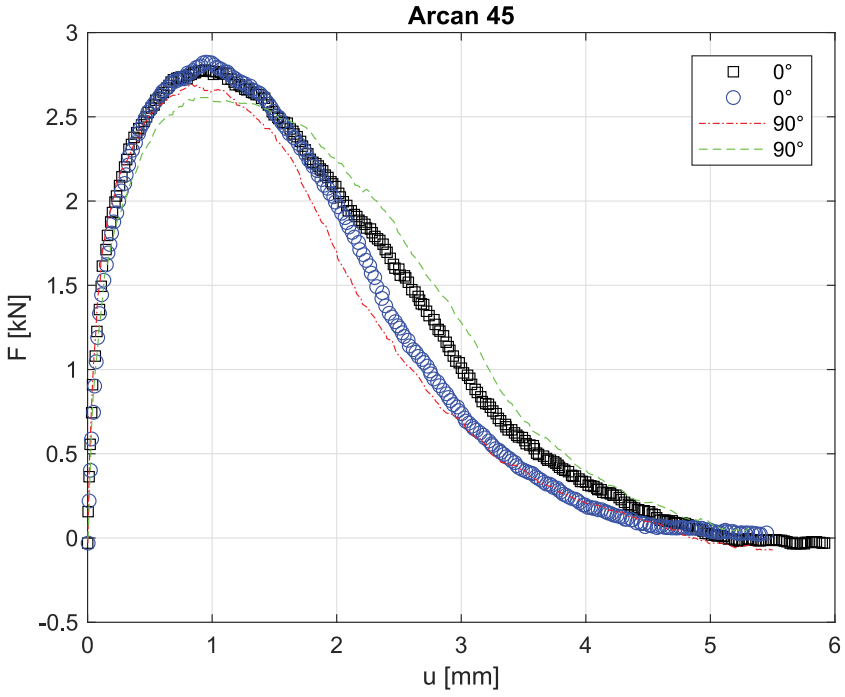
	Peak force (kN)	Displacement at peak force (mm)	Energy (J)
Test 1	2.69	0.84	6.18
Test 2	2.61	0.86	7.41
Mean	2.65	0.85	6.80
Coefficient of mean deviation (%)	1.51	1.63	9.04

however quite similar, as the maximum forces, displacement at failure and energies (Fig. 11, Table 6). The 100*mm/s* experiments are slightly more scattered than the 1*mm/s* ones (and in particular for the displacement at peak force), and the 1*mm/s* can be considered as included in the 100*mm/s* ones. Based on the comparison of the force-displacement curves of the 1*mm/s* and 100*mm/s* tests (Fig. 11), it is thus not possible to conclude about a significant load speed sensitivity of the assembly's strength in this loading speed range.

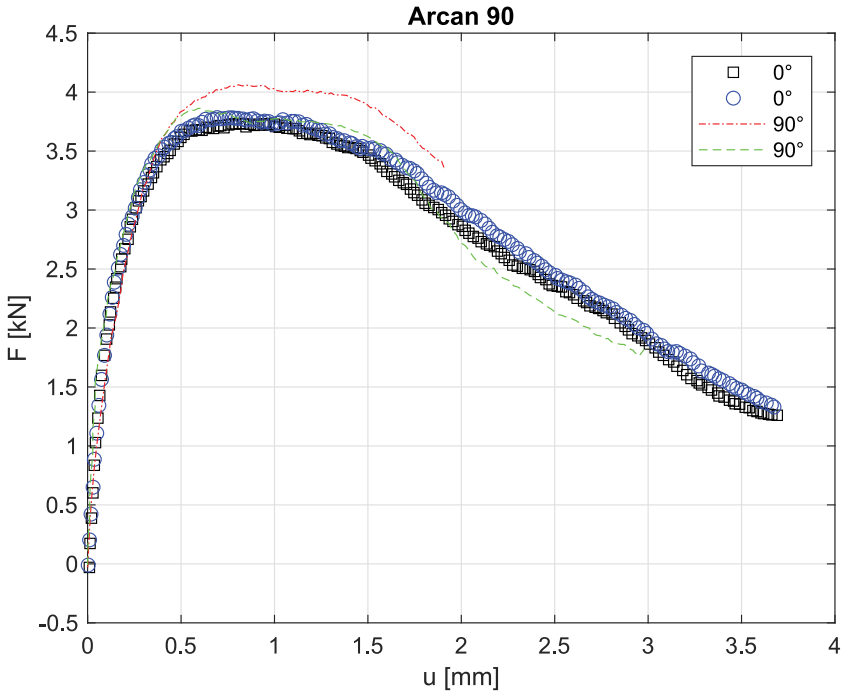
Table 8
90° pure shear tests with 90° fiber orientation.

	Peak force (kN)	Displacement at peak force (mm)	Energy (J)
Test 1	4.06	0.81	6.80
Test 2	3.86	0.59	8.93
Mean	3.96	0.70	7.87
Coefficient of mean deviation (%)	2.52	15.41	13.56

The sensitivity of the force-displacement response to the orientation of the fibers of the laminate was also investigated for the mixed loading case (45°) and for the pure shear loading case (90°). For each loading case, two fiber orientations were tested: 0° and 90°. For the Arcan mixed loading case (45°) the dissipated energy is similar for the 0° and 90° fiber orientations (Table 7), while the peak force and displacement at peak force are slightly lower at 90° than 0°. For the Arcan pure shear loading case (90°) the displacement at peak force and dissipated energy are similar for the 0° and 90° fiber orientations (Table 8), while the peak force is slightly higher at 90° than 0°. Whatever the orientation of the fibers, the force displacement curves for both loading cases also look quite similar, and it is thus concluded that there is no obvious dependency of the strength and failure of the aluminum / Pa66 SPR assembly to the orientation of the Pa66 fibers (Fig. 9).



(a)



(b)

Fig. 9. Effect of fiber orientation on the force displacement responses.

3. Numerical model

This section is dedicated to the modeling of the Arcan experiments. The connector model is presented first. The influence of the material model parameters and of the criteria parameters are then investigated to facilitate the definition of the connector calibration procedure. The SPR assembly model is finally presented and the numerical results obtained are compared to the experiments.

3.1. Connector model

The connector employed is a 2-node generalized spring. The element degrees of freedom are defined in the local frame, and are the relative generalized motions of one node to another: three degrees of freedom in translation $\boldsymbol{u}^t = \{u_1, u_2, u_3\}$.

The variables are two shear forces (f_1 and f_2), a normal force (f_3). Note that $\boldsymbol{x}_3$ is the principal axis of the connector.

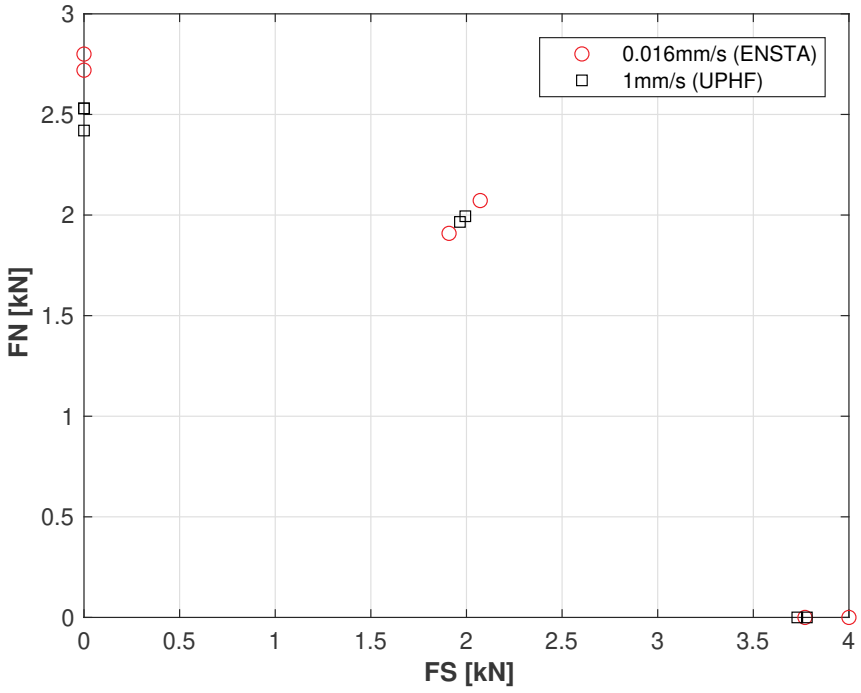


Fig. 10. Maximum force load speed sensitivity depending on the loading angle.

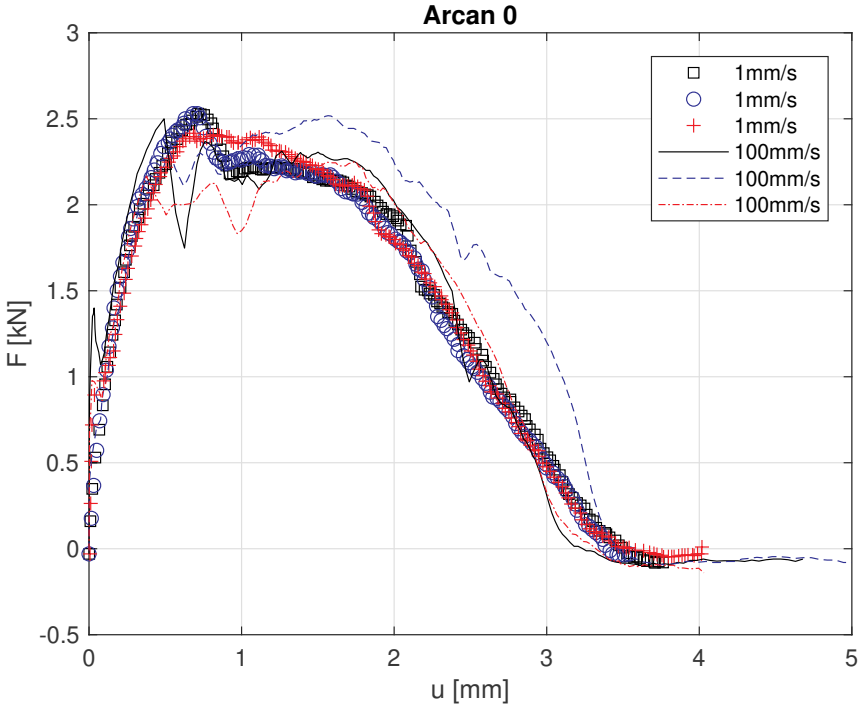


Fig. 11. Load speed sensitivity for a pure tensile loading.

Table 9
Parameters of the connector element.

Elasticity	$D_{11} = D_{22}$	D_{33}
Plasticity	F_0, Q, b	F_{pN}, $F_0 = F_{pS}$, β_p
Damage	F_{iN}, F_{iS}, β_i	u_{fN}, u_{fS}, β_f

The linear elastic stiffnesses of the connector element are assumed to be uncoupled (Eq. (2)). The three components relate forces and displacements.

$$\{f_i\} = [D_{ii}]\{u_i\} \tag{2}$$

with i = 1:3.

The shear stiffnesses are assumed equal: $D_{11} = D_{22}$.

The non-linear behavior of the connector is modeled by a 'plastic' model. The term 'plasticity', is used here to designate a permanent deformation in the broadest sense. It does not refer to the material

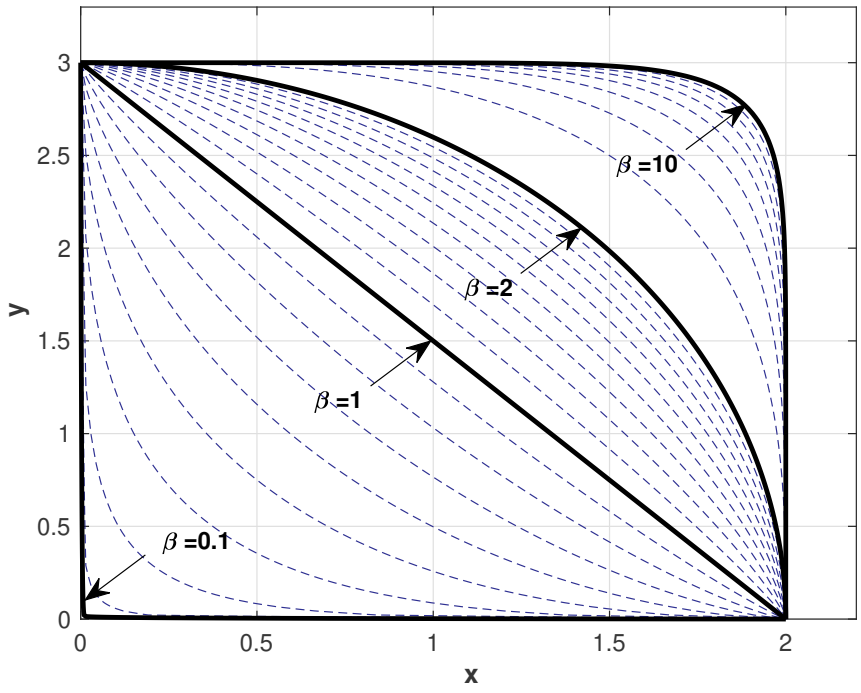


Fig. 12. Evolution of β-norm depending on the value of β, for $X_s = 2$, $Y_n = 3$.

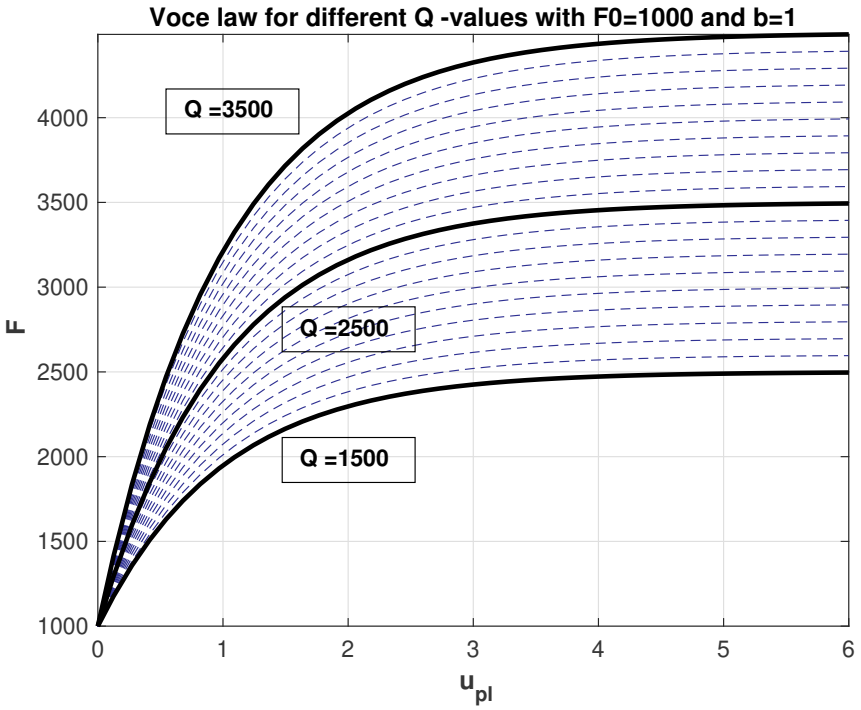


Fig. 13. Voce law depending on the value of Q, for $F_0 = 1000$, $b = 1$.

plasticity theory of the continuum solid mechanics. Note that instead of handling an equivalent stress and a cumulative 'plastic' strain, the model is formulated based on an equivalent generalized force $\bar{F}$ and a permanent relative motion $\bar{u}^{pl}$. The 'plastic' criterion used is given by:

$$\phi(\bar{F}, \bar{u}^{pl}) = \bar{F} - F_H \leq 0 \tag{3}$$

where ϕ is the yield function, $\bar{F}$ is the equivalent generalized force of the connector, and F_H is an isotropic 'hardening' function. When $\phi < 0$ the connector behavior remains elastic, and when $\phi = 0$ 'plastic' flow occurs following an associated flow rule.

$\bar{F}$ in Equation (3) is computed using a potential function P_1. The potential function proposed is a β-norm :

$$\bar{F} = P_1 = \left[\left(\frac{F_N}{F_{pN}} \right)^{\beta_p} + \left(\frac{F_S}{F_{pS}} \right)^{\beta_p} \right]^{\frac{1}{\beta_p}} \tag{4}$$

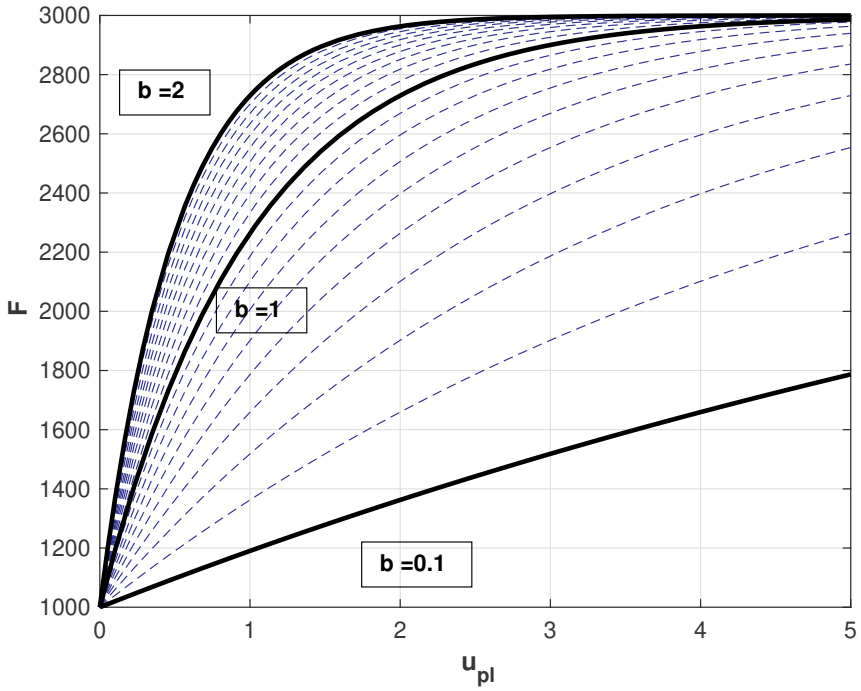


Fig. 14. Voce law depending on the value of b, $F_0 = 1000$, $Q = 2000$.

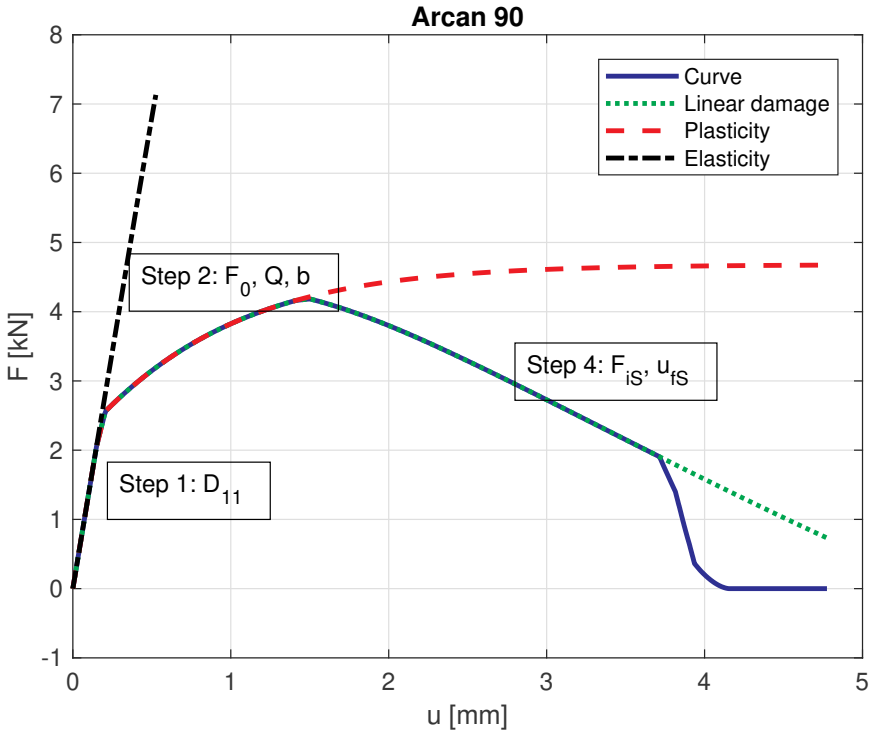


Fig. 15. Calibration steps related to the pure shear experimental curves.

where $F_N = |f_3|$ is the equivalent normal force, $F_S = \sqrt{f_1^2 + f_2^2}$ is the equivalent shear force, F_{pN}, F_{pS} are respectively the tensile plastic limit and the shear plastic limit, and β_p is a β-norm exponent related to plasticity.

The chosen hardening function F_H is an isotropic Voce law:

$$F_H = F_0 + Q(1 - \exp(-b\bar{u}^{pl})) \tag{5}$$

where F_0 is the initial yield equivalent force, Q is the saturation force, and b is a constant.

As for plasticity, damage should not be considered here in a strict sense. It represents the irreversible degradation of the connection. Damage is initiated when the equivalent force reaches the critical force, or threshold, noted F_i:

$$\bar{F} \leq F_i \tag{6}$$

The damage initiation potential P_2 is quite similar to the plastic potential P_1 (Eq. (4)):

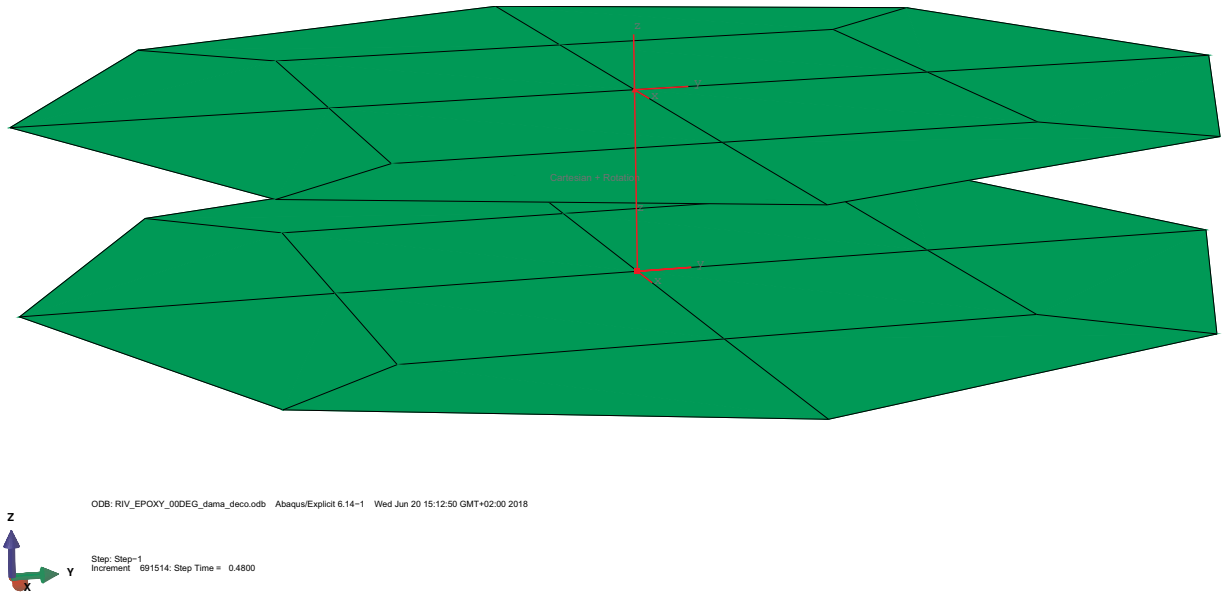


Fig. 16. Arcan numerical model. Aluminum plate on top with a centered connector.

Table 10
Elastic parameters in computations.

	$D_{11} = D_{22}(N/mm)$	$D_{33}(N/mm)$
Elasticity	18000	14000

Table 11
Voce law parameters in computations.

	$F_0(N)$	$Q(N)$	$b(-)$
Voce	2600	1150	9

Table 12
Normalized β-norm criteria in computations.

	Plasticity	*Initiation*	*Failure*
Y_n/X_s	0.66	0.6535	0.75
X_s	2600N	3749.6N	4.0mm
β	1.0	0.875	2.7

$$\bar{F} = P_2 = \left[\left(\frac{F_N}{F_{iN}}\right)^{\beta_i} + \left(\frac{F_S}{F_{iS}}\right)^{\beta_i}\right]^{\frac{1}{\beta_i}} \tag{7}$$

where the subscript i refers to damage initiation while p referred to plastic limit.

When the connector element undergoes irreversible degradation, the equivalent force evolution is as follows:

$$\bar{F}_d = (1 - d)\bar{F} \tag{8}$$

where d is the variable of damage evolution ($0 \leq d \leq 1$) that can be either defined in a linear or tabular way.

When d equals 1, the ultimate failure motion $\bar{u}$ is reached and the connection breaks. $\bar{u}$ is defined as follows:

$$\bar{u} = P_3 = \left[\left(\frac{u_N}{u_{fN}}\right)^{\beta_f} + \left(\frac{u_S}{u_{fS}}\right)^{\beta_f}\right]^{\frac{1}{\beta_f}} \tag{9}$$

where $u_N = |u_3|$ is the equivalent normal displacement, $u_S = \sqrt{u_1^2 + u_2^2}$ is the equivalent shear displacement, u_{fN}, u_{fS}, are respectively the tensile displacement failure limit and the shear displacement failure limit, and β_f is a β-norm exponent related to failure.

The 13 connector parameters are finally summarized in Table 9.

3.2. Some considerations on models

It is proposed to give a closer look to the β-norm criterion that intervenes for plasticity, maximum force and maximum displacement thresholds. The criteria (Eqs. (4), (7), (9)) are of the following general form:

$$\left[\left(\frac{x}{X_s}\right)^{\beta} + \left(\frac{y}{Y_n}\right)^{\beta}\right]^{\frac{1}{\beta}} = 1 \tag{10}$$

where x is the shear axis, y is the tensile axis, X_s represents a shear threshold and Y_n a tensile threshold (Eq. (10)). As presented in Section 3.1, the quantities dealt with can be either of force (Eqs. (4), (7)) or displacement (Eq. (9)) nature.

A β-norm criterion can also be considered in a form that is normalized with respect to a component. For example, here, the β-norm is normalized with respect to the shear axis x:

$$\left[x^{\beta} + \left(\frac{y}{Y_n/X_s}\right)^{\beta}\right]^{\frac{1}{\beta}} = X_s \tag{11}$$

In order to evaluate in a better way how the β-norm criterion works (Eq. (10)), it is proposed to consider the particular case in which $X_s = 2$ and $Y_n = 3$. The parameter β is varied from 0.1 to 2 with a step of 0.1, and from 2 to 10 with a step of 1, see Fig. 12.

Note that the particular cases $\beta = 2$ and $\beta = 1$ simply correspond to an ellipse and a straight line, respectively. Otherwise, the shape of the criterion can be quite general. It can also be seen that whatever the β value, X_s and Y_n remain exactly equal to 2 and 3, respectively. It means that in a β-norm criterion, the identification of X_s and Y_n can be decoupled from that of β.

The influence of the parameters of the non-linear Voce hardening law (Eq. (5)) can also be looked at. It is proposed to consider a case in which $F_0 = 1000$, $b = 1$ and the parameter Q is varied from 1500 to 3500 with a step of 100 (Fig. 13). Another case is considered in which $F_0 = 1000$, $Q = 2000$ and the parameter b is varied from 0.1 to 2 with a step of 0.1 (Fig. 14). It appears that the parameter Q drives the maximum force reached F_∞, so that $F_\infty = F_0 + Q$. The parameter b drives

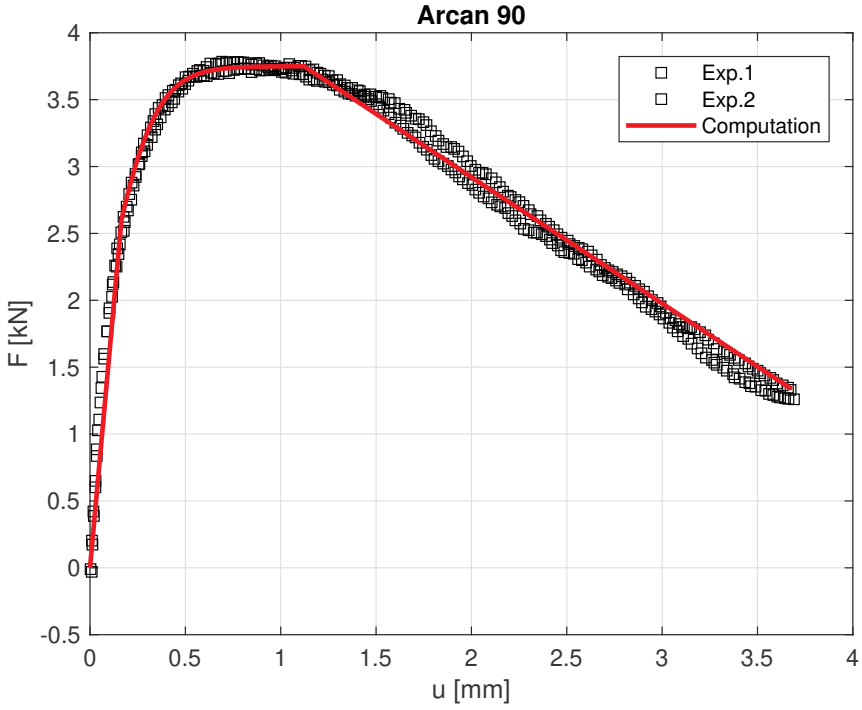


Fig. 17. Pure shear Arcan test / simulation.

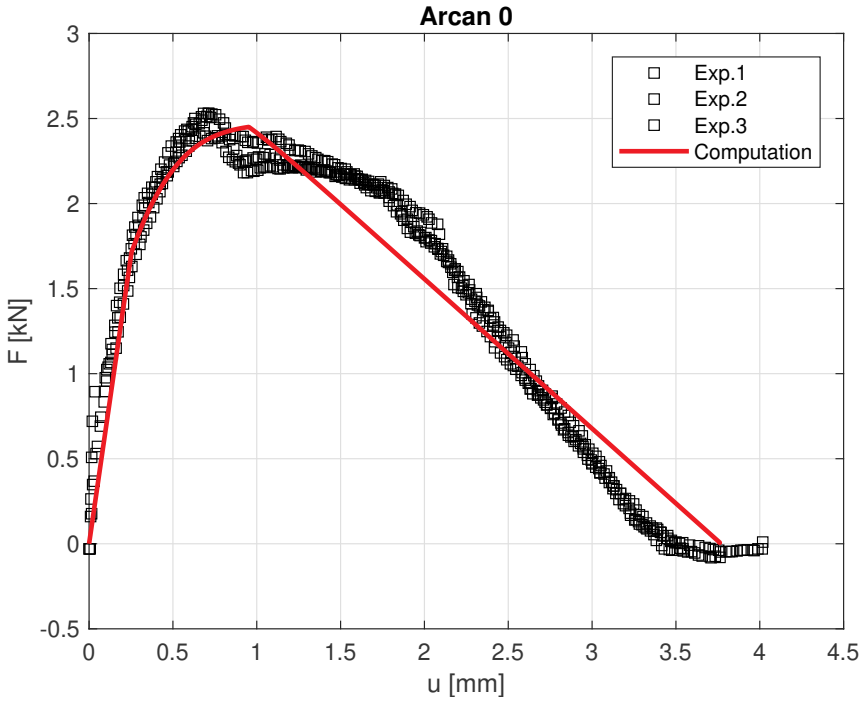


Fig. 18. Pure tensile Arcan test / simulation.

the curvature, and can in practice delay the reaching of the maximum force F_∞.

3.3. Connector calibration procedure

A general procedure is proposed to calibrate the linear elastic, non-linear Voce hardening law, β-norm criteria, and tabular damage of the connector model based on Arcan pure and mixed tensile/shear experiments.

The proposed connector calibration procedure is sequential and is as follows (Fig. 15):

1. Calibrate the shear $D_{11} = D_{22}$ and tensile D_{33} stiffnesses based on the pure shear and pure tensile experiments, respectively,
2. Calibrate Voce law parameters ($F_0(=F_{pS})$, Q, b) based on pure shear experimental curves,
3. Calibrate the plastic limit criterion (F_{pN}/F_{pS}, β_p) based on pure tensile and mixed tensile shear plastic thresholds,
4. Calibrate the damage parameters (F_{iS}, u_{fS}) based on pure shear experimental curves,

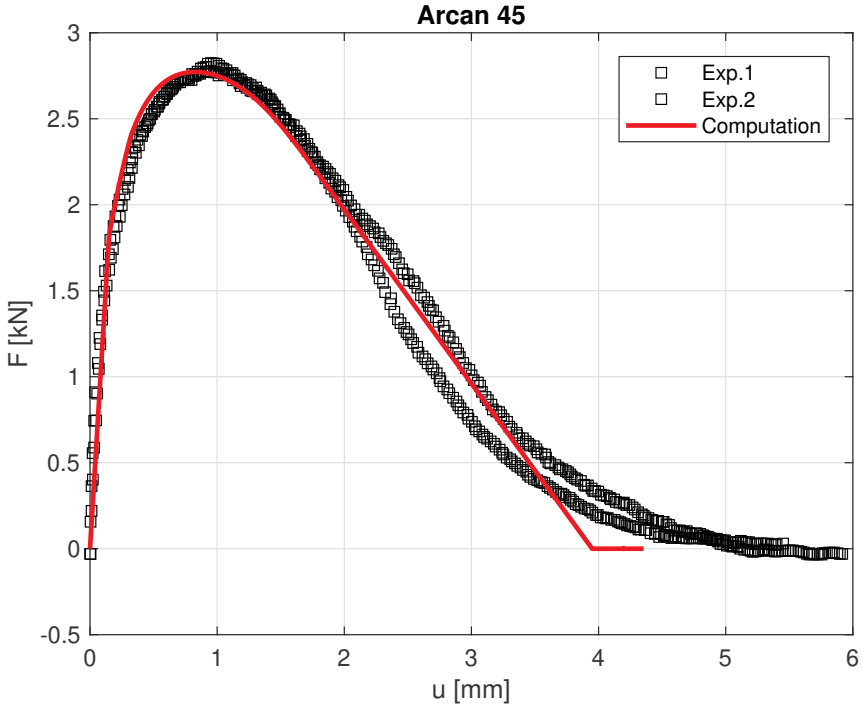


Fig. 19. Mixed tensile / shear Arcan test / simulation.

Table 13
Prediction of the numerical model for some key values.

	0°	45°	90°
Peak force (kN)	2.45	2.77	3.75
Displacement at peak force (mm)	0.95	0.83	1.12
Energy (J)	5.26	6.68	10.12

5. Calibrate the damage initiation criterion (F_{iN}/F_{iS}, β_i) based on pure tensile and mixed tensile shear damage initiation thresholds and the failure criterion (u_{fN}/u_{fS}, β_f) based on pure tensile and mixed tensile shear failure thresholds.

The substep dedicated to the calibration procedure of a β-norm criterion is as follows, based on the considerations of Section 3.2 and irrespectively of the nature of the criterion considered:

1. Get the previously calibrated shear limit parameter X_s,
2. Calibrate the tensile limit parameter Y_n in the pure tensile Arcan computation based on the pure tensile experimental limit,
3. Calibrate the exponent β in the mixed tensile/shear Arcan computation based on the mixed tensile/shear experimental limit.

3.4. Assembly model

To model the SPR Arcan experiments, a flat aluminum plate is connected to a flat PA66 plate by a single connector element. Only the free part of the plates is modeled (see Section 2, Figs. 4, 16). The circumference of the PA66 plate is fixed. An imposed displacement boundary condition is applied to the circumference of the aluminum plate to model pure tensile, pure shear, and mixed tensile/shear (45°) loadings. The PA66 and aluminum plates are both 2 mm thick. The aluminum and PA66 plates are modeled using large strain reduced integration Reissner-Mindlin shell elements. The mesh size is about 5mm. The material properties of aluminum are defined as follows: density $\rho = 2700kg/m3$, Young's modulus $E = 75000$MPa, Poisson's coefficient $\nu = 0.33$. The hardening is described by a tabular law. The material properties of PA66 are defined as follows: density $\rho = 1470kg/m3$, Young's moduli $E_1 = E_2 = 27000MPa$, shear moduli $G_{12} = G_{13} = G_{23} = 2600MPa$, Poisson's ratio $\nu_{12} = 0.25$. The computations are performed using Abaqus explicit.

The calibration procedure presented in Section 3.3 is applied to the Arcan PA66-aluminum self piercing rivets experiments (Section 2). Note that a direct identification procedure is run first based on the experimental Arcan force-displacement responses of the assembly. It provides initial parameter values as a starting point for calibration.

The calibrated parameter values of the connector element are summarized in Tables 10, 11, 12.

3.5. Numerical results

All Arcan computation responses appear to be in agreement with the experiments in terms of linear and non-linear stiffnesses, maximum forces, damage evolution, displacement at failure, and energy (Figs. 17, 18, 19). The peak forces and dissipated energies are particularly well predicted by the numerical model (Table 13). More error is observed on the displacement at maximum force. Note that the authors consider the displacement at maximum force a less important feature than maximum force, displacement at failure and dissipated energy. Other priorities could be decided in the calibration process.

In fact considering the connection model (linear elasticity, non-linear hardening, linear damage) (Fig. 15), the 0° experimental response in particular is difficult to reproduce due to the post-peak short force drop and the slowly decaying plateau that follows. The force drop cannot be taken into account without enriching the connector description (for example using tabular damage).The 90° experimental response also features a slowly decaying plateau. Since the plateau are described thanks to Voce law in the numerical model, it can only be slowly increasing. It explains the compromise that is met to the detriment of the displacement at peak force in the numerical model.

Apart from this detailed analysis of the connection model, the overall agreement is really satisfactory and thus validates both the connection model and its parameters for the modelling of aluminum Pa66 arcan experiments.

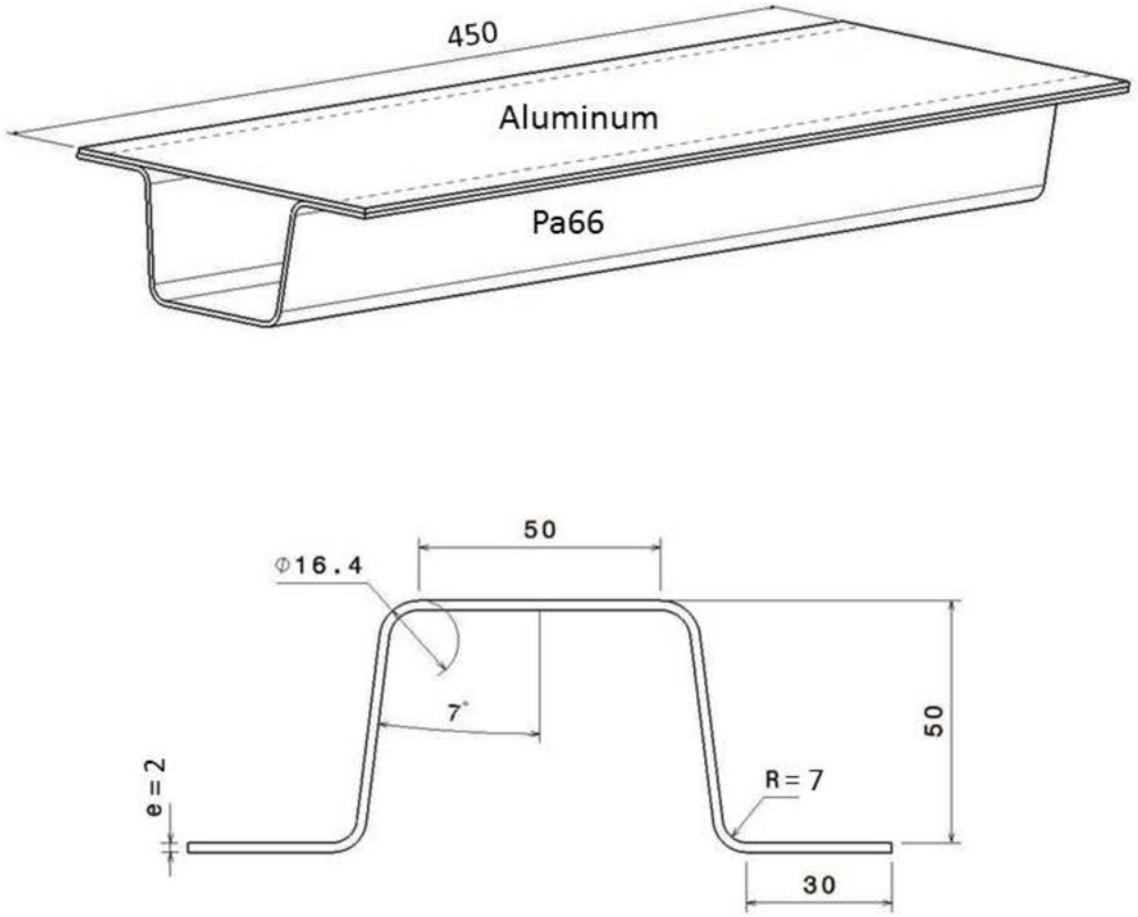


Fig. 20. Single hat component geometry.

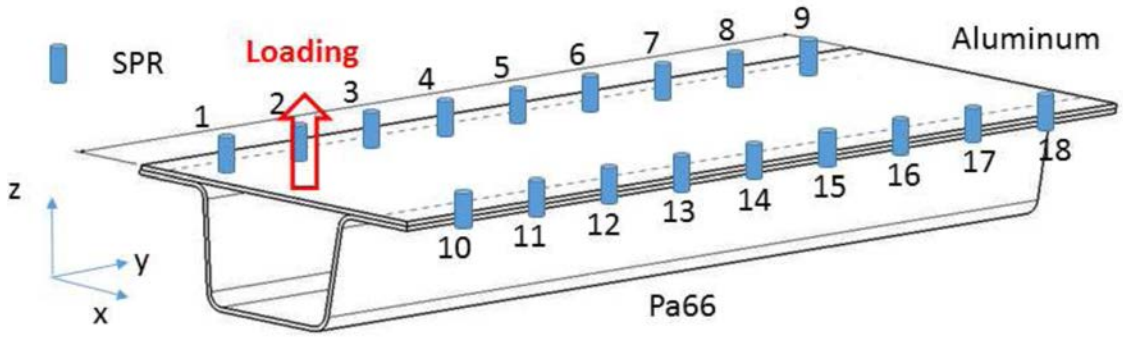


Fig. 21. Numbering of component SPR connections.

4. Single hat component tests and modeling

Single hat component structural experiments are presented in this section with the corresponding numerical simulations. In component tests, multiple connections are involved, and they are loaded in a more complex way than in Arcan tests. These tests are thus more representative of the structural behavior of connections than the Arcan ones.

4.1. Experiments

The component is made of an omega-shaped PA66 part assembled with a flat aluminum plate (Fig. 20) by 2 rows of 9 SPR spaced one another by 50*mm* (Fig. 21).

The testing rig is composed of an intermediate part on which the single hat component is fixed, of an arm that loads the flat aluminum plate, and of supports (Fig. 22). A clamping rod ensures that the component is fixed to the intermediate part. The intermediate part is linked to the ground (supports) by means of two Michigan 13.5kN - Type TR3D-A 3Klbs multi-axial load cells. The loading is applied by an arm to the flat aluminum plate by means of an intermediate flange screwed on it. A revolute joint links the arm to the flange. The loading arm is equipped with a mono-axial load cell (MEAS 25kN - Type FN3042).

The loading is applied to the component with an inclination angle of 20° with respect to the flat aluminum plate and is applied at one of its free ends (Fig. 22). Two loading speeds have been investigated: a low dynamic speed (5mm/s) and a fast dynamic speed (1500*mm/s*).

The Fig. 23 illustrates the deformation mechanisms of the component for a loading speed of 1500*mm/s*. In fact, the aluminum plate tends to roll up when the separation propagates from rivet line to rivet line.

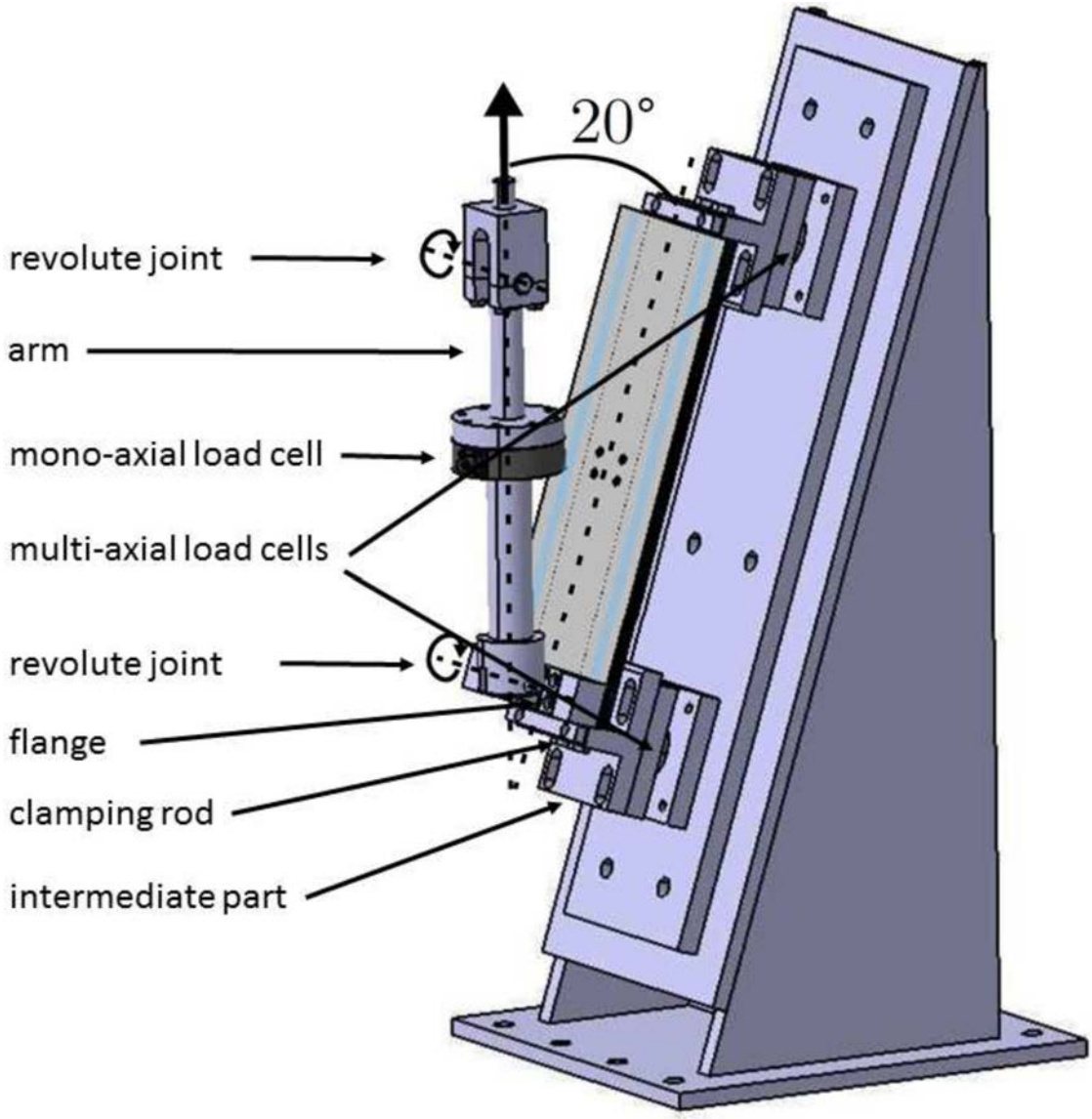


Fig. 22. Experimental setup for the component experiment.

As expected, the left rivet line is loaded first until it breaks. Then the aluminum plate deforms and the second line of rivets is loaded until it breaks. However, it appears that most of the time, the rivets of a rivet line do not fail simultaneously (Table 14, Fig. 21). Moreover, the SPR failure sequence is not necessarily the same depending on the experiment considered. It is expected to come from variations in the properties of the connections which are not exactly the same due to variations in the process or else.

The force-displacement curves are shown in Fig. 24. Note that the repeatability of the force-displacement curves is quite good. The curves exhibit two distinct peak forces. A sudden force drop is observed after each peak force corresponding to the failure of a rivet line. The force tends to zero after each peak, meaning that the plate is quite free to move at that time. It is then followed by plate bending (roll-up) and load transfer to the next rivet line. Two distinct energy absorption phases are observed, corresponding to the successive failure of the two rivet lines. The connections thus play a significant role in the component experiment. At 5mm/s, it appears that the two rivet lines fail for a displacement of 25.63mm and 85.48mm in mean, respectively, with corresponding efforts of 1.70 and 2.05kN in mean. The energy dissipated at first peak is 30.10J and the total dissipated energy 103.59J in mean (Table 15). The corresponding values at 1500mm/s are as follows: the two rivet lines fail for a displacement of 30.79mm and 91.00mm in mean, respectively, with corresponding efforts of 1.79 and 2.16kN in mean. The energy dissipated at first peak is 36.44J and the total dissipated energy 114.24J in mean. The maximum forces, displacements at peak force and dissipated energies are thus slightly higher in the 1500mm/s case. The sensitivity to the loading speed thus appears to be slightly more significant in the component experiment in the range 5mm/s - 1500mm/s than in the (pure tensile) Arcan tests in the range 1mm/s - 100mm/s (Fig. 11). It might either be caused by a viscous effect that activates in this range or an inertia effect due to a higher mass in the component experiment than in the Arcan ones.

4.2. Modeling

To model the component experiments, a flat aluminum plate is connected to an omega-shaped PA66 plate by two rows of 9 connectors each. The mesh size is 5 mm. A steel flange is meshed with tetraedra elements. The whole mesh features 19,383 elements (Fig. 25). The global y-axis is aligned with the length of the aluminum plate, x-axis is along its width, and z-axis is normal to the aluminum plate (Fig. 21).

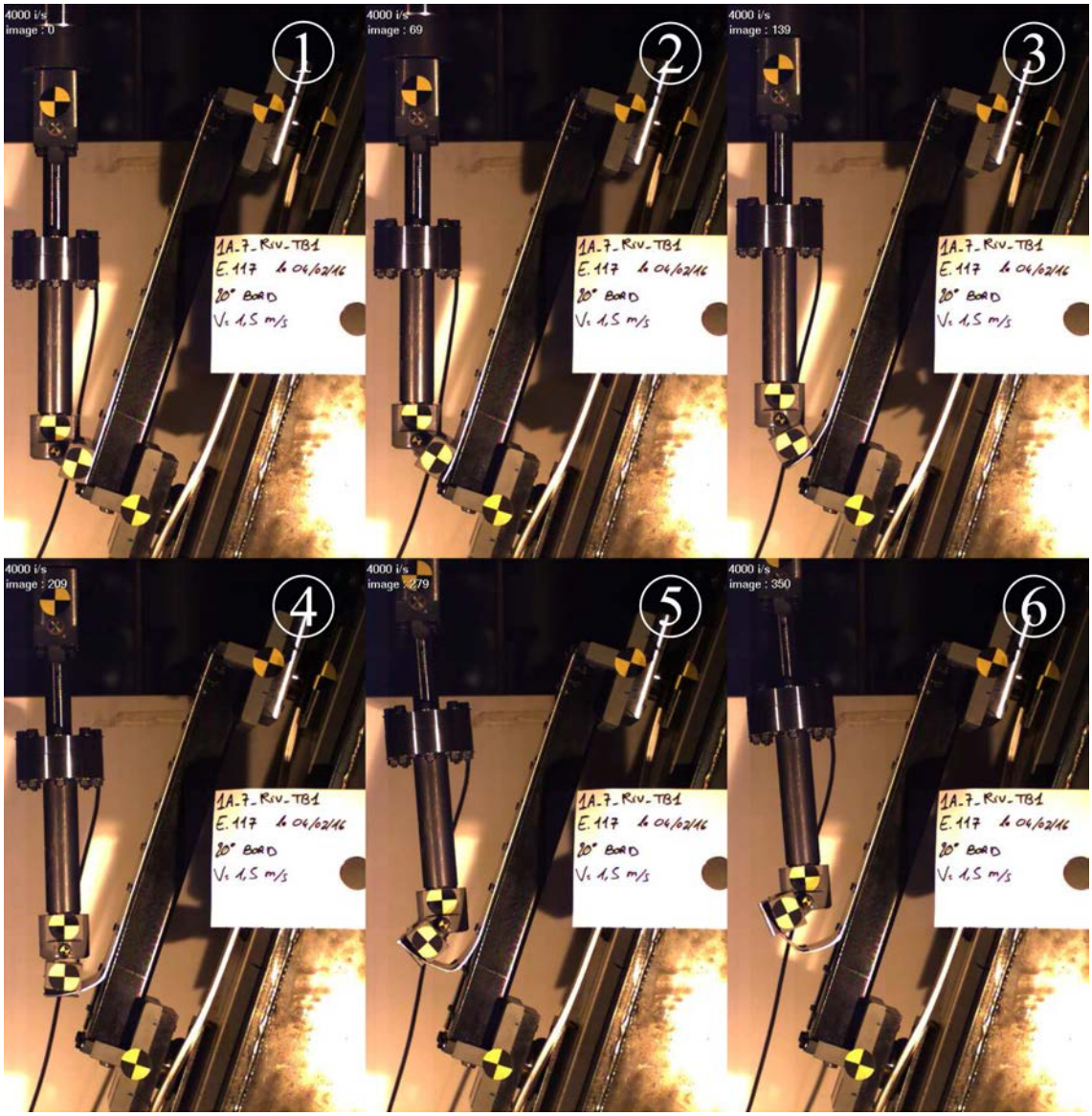


Fig. 23. Deformation and failure mechanisms of the component experiment.

Table 14
Component experiments SPR failure sequence.

	SPR failure sequence	Corresponding times (ms)
Test 1 (1500mm/s)	1 ; 10 ; 11 ; 2	26.5 ; 31.8 ; 64.0 ; 65.3
Test 2 (1500mm/s)	10 ; 1 ; 11 ; 2	23.8 ; 25.7 ; 61.2 ; 62.8
Test 3 (1500mm/s)	1 ; 10 ; 2 ; 11	26.0 ; 28.0 ; 65.0 ; 65.0

The finite element type and the PA66 and aluminum material properties used in the Arcan computations remain unchanged (Section 3.4). The material properties of the steel flange are as follows: $\rho = 7800kg/m^3$, $E = 210000$MPa, Poisson's coefficient $\nu = 0.3$.

The bottom of the PA66 omega is fixed. The steel flange is rigidly linked to the flat aluminum plate. A prescribed tabular displacement corresponding to the recorded experimental one for test 1 is imposed to the steel flange. It is inclined -20° with respect to x-axis

A unique connector card is defined and assigned to the 18 connectors of the model. The parameter numerical values are those identified in Section 3.4 (see Tables 10, 11, 12).

4.3. Validation

The deformed shape of the component is presented in Fig. 26. It is in agreement with the experimental one, since two rivet lines only have failed and that the aluminum plate rolls up. More precisely, as expected, the rivets belonging to the same rivet line fail simultaneously in the numerical simulation. It holds both for the first rivet line (1; 10) and the second rivet line (2, 11). In the experiment, the rivets of the second rivet line fail simultaneously, but rivet 10 fails slightly earlier than rivet 1 in the first rivet line (see Test 1 in Table 14).

Fig. 27 shows a comparison between the experimental and numerical results. The peak force estimates in particular are quite good in the numerical model, but the peak forces occur for displacement values slightly lower than in the experiments. Indeed, in the computation, the two rivet lines fail for a displacement of 27.58mm and 90.65mm in mean, respectively, with corresponding efforts of 1.86 and 2.24kN. The energy dissipated at first peak is 27.58J and the total dissipated energy 101.98J in mean (see Table 16). In the experiment, the two rivet lines fail for a displacement of 30.79mm and 91.00mm in mean, respectively, with corresponding efforts of 1.79 and 2.16kN in mean. The energy dissipated at first peak is 36.44J and the total dissipated energy 114.24J

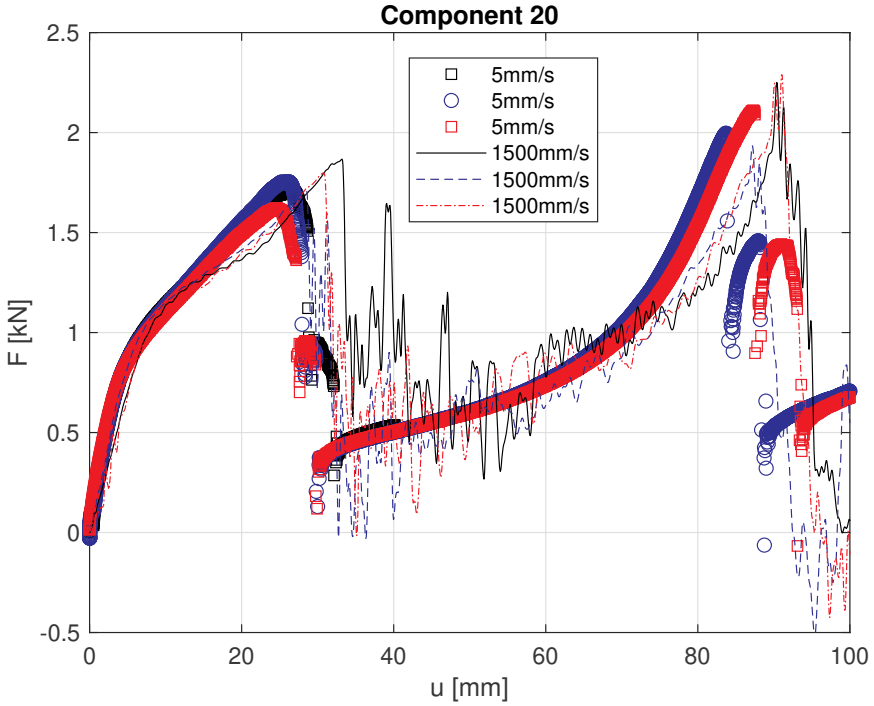


Fig. 24. Force-displacement response of component experiments.

Table 15
Component experiments key values.

	Peak force (kN)	Displacement at peak force (mm)	Energy (J)
	*Peak*1; *Peak*2	*Peak*1; *Peak*2	*Peak*1; *Total*
Test 1 (5mm/s)	1.72 ; –	26.35 ; –	31.29 ; –
Test 2 (5mm/s)	1.75; 2.00	26.00; 83.66	31.14; 102.48
Test 3 (5mm/s)	1.62; 2.11	24.55; 87.30	27.87; 104.71
Mean (5mm/s)	1.70; 2.05	25.63; 85.48	30.10; 103.59
CMD (5mm/s) (%)	2.96; 2.78	2.81; 2.13	4.95; 1.08
Test 1 (1500mm/s)	1.87; 2.25	33.20; 90.38	40.39; 124.44
Test 2 (1500mm/s)	1.72; 1.93	28.44; 87.19	33.31; 104.50
Test 3 (1500mm/s)	1.80; 2.29	30.73; 91.00	35.62; 113.76
Mean (1500mm/s)	1.79; 2.16	30.79; 89.53	36.44; 114.24
CMD (1500mm/s) (%)	2.86; 6.91	5.22; 1.74	7.22; 5.96

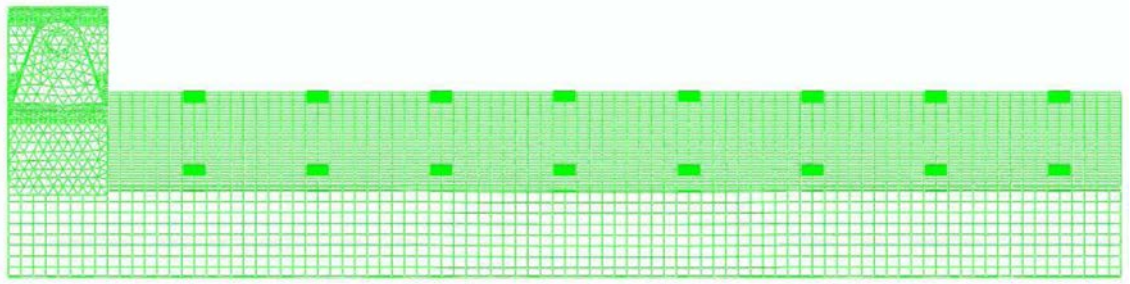


Fig. 25. Mesh of the component, boxes corresponding to connectors.

in mean (see Table 15).

It can also be interesting to post-process the mode mix ratio experienced by the connectors of the component during the computation. The mode-mix ratio Φ is equal to 1 for pure tensile loading and a value of 0 for pure shear loading:

$$\Phi = \frac{2}{\pi} tan^{-1}\left(\frac{F_N}{F_S}\right) \tag{12}$$

For example the connector 1 experiences both shear-dominated and tensile-dominated values of the mode mix ratios during the component experiment (Fig. 28). The mode mix ratio of connectors of a same rivet line (1;10 and 2;11, respectively) is the same. However, the mode mix ratios of the connectors of the first rivet line and the second one are significantly different. Connector 2 also experiences both shear-dominated and tensile-dominated mode mix ratios. This is not shown here for the sake of conciseness.

Since the connectors experience both tensile and shear dominated mode mix ratio values and that the overall agreement is good between

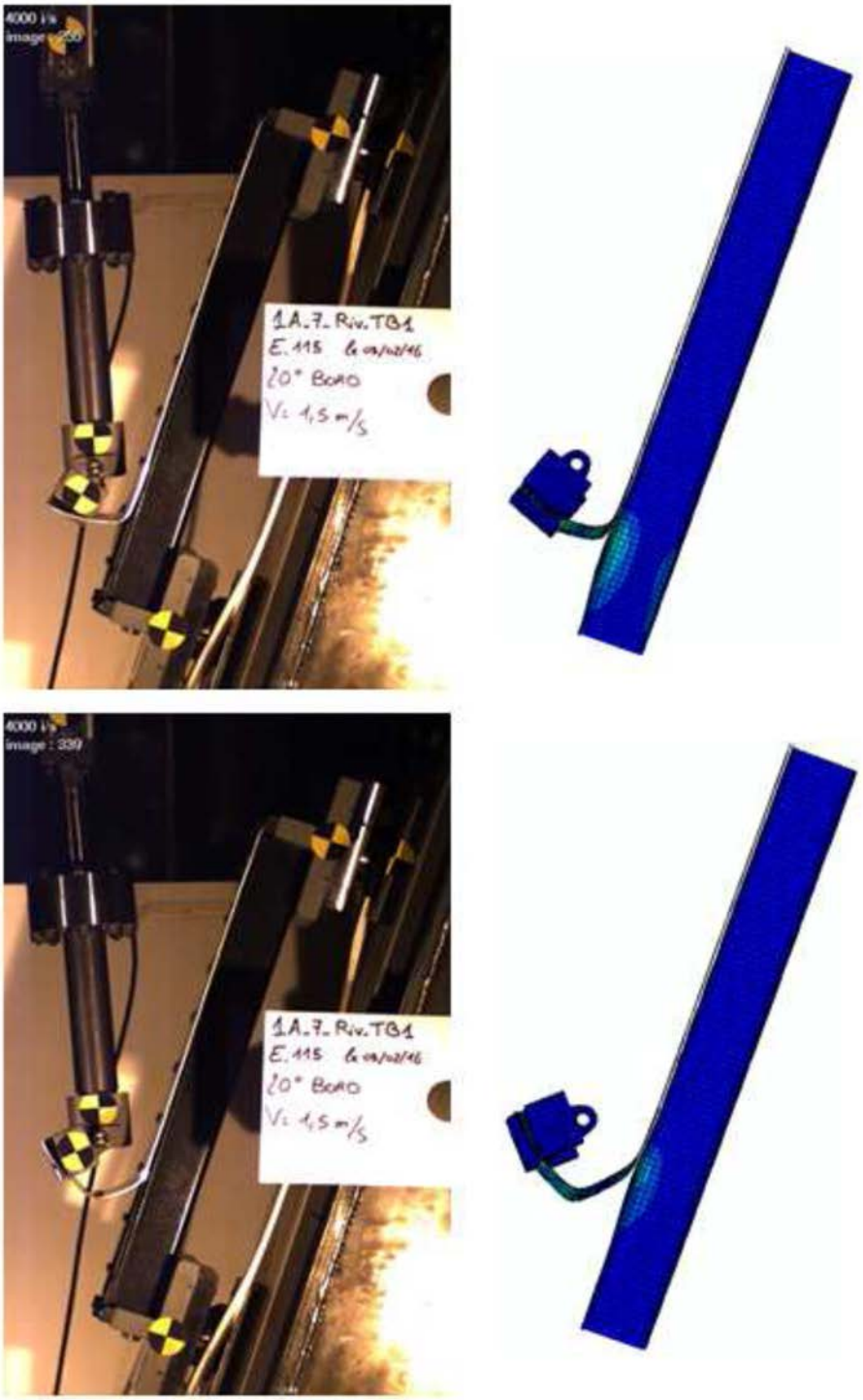


Fig. 26. Comparison of experimental and numerical deformed shapes.

the computation and the component experiments using the parameters calibrated in the Arcan experiments (Section 3.4), these parameters are validated.

4.4. Comments

For the aluminum - PA66 self-riveted assembly, the parameters have been calibrated on pure and mixed Arcan tests, and validated with respect to component experiments.

In fact, a single set of connector parameters allows obtaining a quite good agreement between pure tensile Arcan, pure shear Arcan, mixed tensile shear Arcan, single hat component experiments and numerical simulations. Note that the set of parameters allowing this kind of result may be not unique from an engineering standpoint.

The connector model employed is able to represent the mechanisms occurring in the assembly at a macroscopic level. Note that some plate material effects in particular may be indirectly taken into account in the connector parameters. This is the reason why using a simplistic description of the plate materials can be sufficient to obtain a good macroscopic response agreement with many experiments.

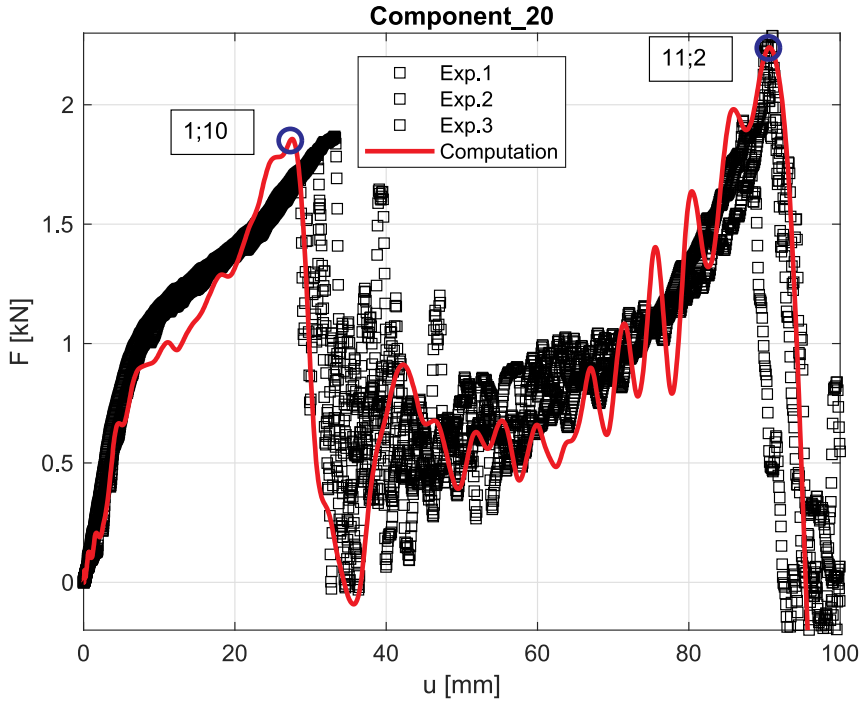


Fig. 27. Comparison of experimental and numerical force-displacement curves.

Table 16
Component computation key values.

	Peak force (kN)	Displacement at peak force (mm)	Energy (J)
	*Peak*1; *Peak*2	*Peak*1; *Peak*2	*Peak*1; *Total*
Computation	1.86 ; 2.24	27.58 ; 90.65	33.55 ; 101.98

The mesh size used in computations (5mm) is representative of the mesh sizes used for the simulation of full scale automotive structures in industry. Finer meshes may help obtaining even better results (more accurate plate bending for example), but would not be affordable in full-scale structural computations.

Several models could be chosen to model plasticity in the connector model instead of Voce hardening law. Indeed, a perfect plastic description, a multilinear description or hardening laws such as Hollomon or Ludwik laws could be envisaged. Perfect plasticity can be quite restrictive, in particular if a non-linear part is present between linear

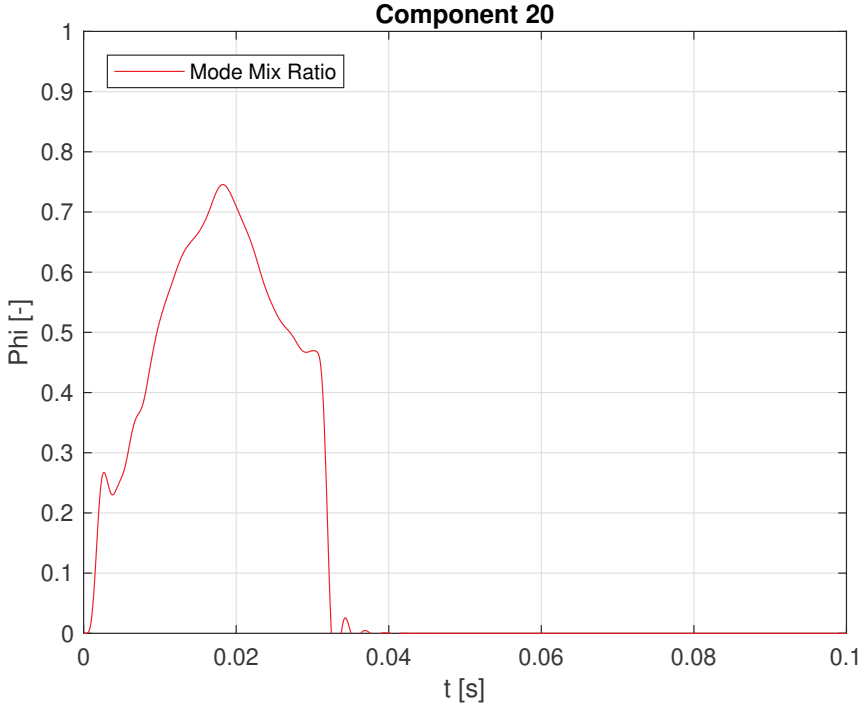
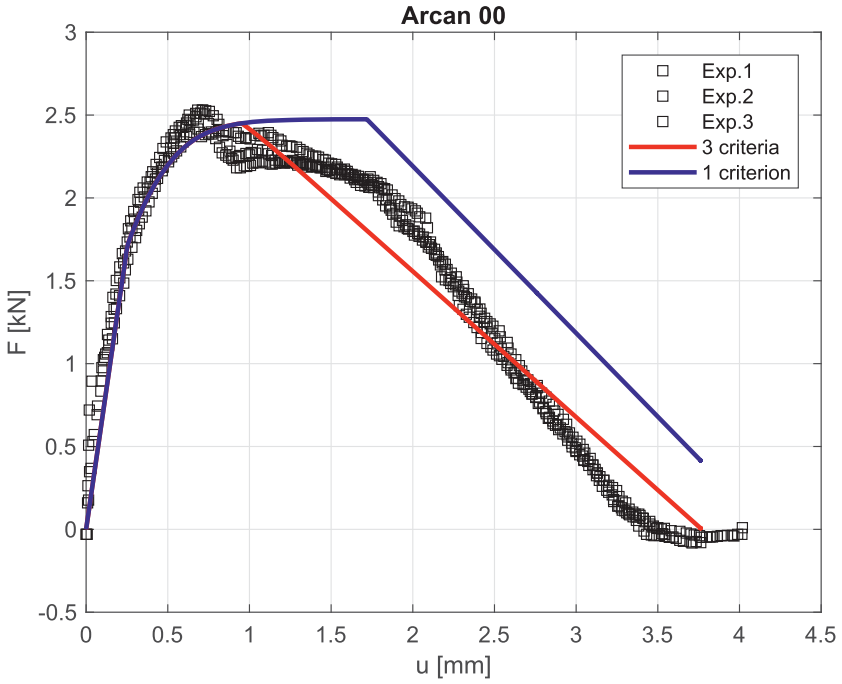
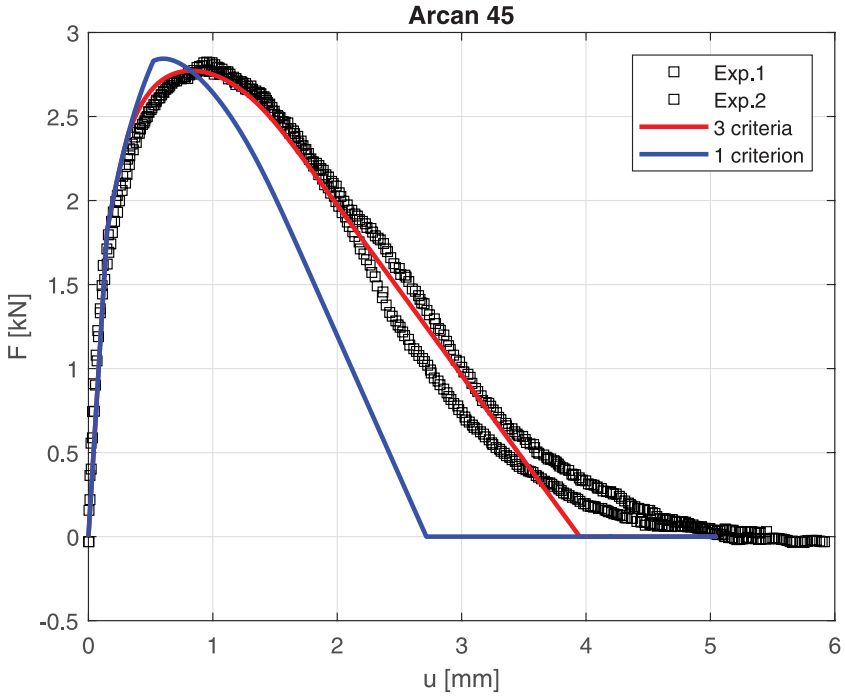


Fig. 28. Mode Mix ratio in connector 1.



(a) Arcan 0



(b) Arcan 45

Fig. 29. Comparison of numerical/experimental agreement depending on the number of criteria.

elasticity and a flat plateau in the experimental response. Multilinear descriptions can describe any shape of curve. However, they can be either quite sharp or costly in terms of unknowns, since each point can represent unknowns to be identified. Hardening laws are less versatile than multilinear descriptions but are smooth and quite cheap in terms of unknown parameters. The number of unknowns of the model is to be taken into account if automatic identification of the model parameters is aimed at. The type of hardening law should be chosen depending on the curve to be described. Note that Voce law is advantageously used here to benefit from both a non-linear hardening part and a flat plateau part to describe the 90° Arcan response (see Fig. 17). It seems that this model will be able to represent self-piercing riveted assembly Arcan responses as long as the hardening (curvature of the non-linear part of the response) on the one hand and the damage evolution on the other hand are sufficiently similar whatever the loading angle. Indeed, the hardening and damage evolution parameters are independent of the loading angle, while the criteria on the contrary depend on the loading angle.

When modelling the aluminum-Pa66 SPR Arcan experiments, a connector model featuring a single criterion was used at first. It corresponds to constraining $F_{pN}/F_{pS} = F_{iN}/F_{iS} = u_{fN}/u_{fS}$ and $\beta_p = \beta_i = \beta_f$ in the model proposed (see Sections 3.1 and 3.2). In fact, with a single criterion, the comparison between Arcan computations and experiments was not satisfactory for all angles. To improve the Arcan models, the authors came to the idea to separate the plasticity, damage initiation, and failure criteria. Fig. 29 shows a comparison of the results obtained with the single criterion model (here for example using the numerical values of the plastic criterion for all criteria) and with the three criteria model. In the case of pure tensile (Fig. 29(a)) and mixed tensile-shear (Fig. 29(b)), the responses are significantly different using a single criterion or three criteria. For pure tensile, even if the values used for damage initiation are quite similar in the single criterion (0.66) and the three criteria (0.6535) models (see Table 12), the responses are quite different (Fig. 29(a)). In fact, it is caused by the combination of the force plateau and of the force-based damage initiation criterion. In such a case, damage initiation is quite sensitive to the force numerical value. For mixed-tensile shear, the responses are different (Fig. 29(b)) because the β-norm values are significantly different (in particular the β-values) for the single criterion and three criteria models (see Table 12). Since the β-norms of the three criteria model are normalized with respect to shear in the methodology proposed (see Sections 3.2 and 3.3), the single criterion and three criteria models provide the same numerical results in the case of pure shear, and are thus not presented. Finally, to the authors opinion, the three criteria connector model should be preferred when modeling a new SPR material couple. The identification of the model parameters will indicate (if the values of the three criteria are sufficiently close) if a single criteria connector can be used.

Note also that Bier et al. [32] seem to be the first authors to propose the use of separate plastic, damage initiation and failure criteria in a SPR connector model. However, in their case, a single criterion model gave satisfactory results to model Arcan-like experiments, while the results were unsatisfactory for peeling tests [31]. They thus proposed the use of three criteria together with weighting parameters and a load symmetry factor in order to improve the modelling of the peeling tests.

The connector model of the commercial software Abaqus allows modelling quite different point-to-point connections [35]. It can for example model connections such as revolute or cardan joints occurring in automotive suspension systems. It can also be used to apply loads or boundary conditions to a model. It can finally be used to model force-displacement or force-velocity behaviors. Both coupled and uncoupled behaviors can be defined. Elasticity, plasticity, damping, damage, failure elementary blocks may be associated in a rheological way (i.e., in series or in parallel) [36]. The behavior elementary blocks are not limited to appear only once in the rheological model of the connector neither. Also the criteria of the coupled behaviors can be shaped by the user and not only selected among different possibilities. Note that the model employed here for the aluminum-Pa66 SPR assembly can be defined using the standard features of the versatile connector model of Abaqus software, i.e., it does not require any sub-routine, user-material, or user-element to be programmed.

Note that the model employed here has been successful in modelling aluminum-Pa66 composite and for metallic-metallic SPR assemblies [32]. As a consequence, other metallic-metallic models of the literature may be successful in the modelling of the aluminum Pa66 assembly. Some prospects will concern the testing of other metallic-composite SPR assemblies to evaluate if this model still provides satisfactory results or if the rheological model of the connector requires modifications.

5. Conclusion

The strength and failure of two sheet aluminum-PA66 composite SPR assemblies have been characterized using pure and mixed tensile/shear single connection Arcan experiments. The maximum force and the dissipated energy increased with the loading angle. These experiments have not shown significant load speed sensitivity, nor significant fiber orientation sensitivity. Many similarities have been observed between the behaviour and failure of aluminum-PA66 SPR assemblies and that of the aluminum-aluminum ones. The failure modes Fs1 and Fs5 have been observed in particular. Other metallic / composite material couples and / or thicknesses could be tested to evaluate if the other metallic SPR assembly failure modes Fs2, Fs5, that have not been observed yet for the current configuration, would be also observed. Multiple connection component experiments have also been performed at 5mm/s and 1500mm/s. The maximum forces and dissipated energies slightly increased at 1500mm/s. Both tensile and shear dominated mode mix ratio values were experienced by the connections.

A 13-parameter SPR connector model has been employed featuring a linear elastic description, a Voce hardening law, a linear damage evolution, three β-norm criteria respectively used for the irreversible deformation threshold, the maximum force and the failure. A calibration procedure, based on an analysis of the hardening law and criteria, decouples the calibration of the pure tensile / shear contributions from the mixed tensile / shear ones. The parameters of the connector model are calibrated using Arcan experiments and validated using component experiments. The numerical results have shown a good agreement not only in the pure tensile, pure shear, and mixed tensile shear Arcan experiments, but also in the omega-shaped component one. This model thus provides a good description of the strength and failure of the aluminum-PA6 composite self-piercing joint at a macroscopic level. Other material couples could be employed to evaluate the generality of the presented SPR connector model. Some prospects also concern the automatic identification of the proposed SPR model parameters.

Acknowledgements

The present research work has been supported by the 'Programme Vehicule du Futur' from 'Projets d'Investissement d'Avenir' coordinated by ADEME (project FASTLITE), the Nord-Pas-de-Calais Region, the European Community, the Regional Delegation for Research and Technology, the Ministry of Higher Education and Research, and the National Center for Scientific Research. The authors gratefully acknowledge the support of these institutions. The authors gratefully thank the reviewer for pointing out the existence of the work of M. Bier and S. Sommer.

References

[1] Porcaro R, Hanssen A, Langseth M, Aalberg A. The behaviour of a self-piercing riveted connection under quasi-static loading conditions. Int J Solids Struct 2006;43(17):5110–31.
[2] Sun X, Stephens E, Khaleel M. Fatigue behaviours of self-piercing rivets joining similar and dissimilar sheet metals. international journal of fatigue. Int J Fatigue 2007;29:370–86.
[3] Sun X, Khaleel MA. Dynamic strength evaluations for self-piercing rivets and resistance spot welds joining similar and dissimilar metals. Int J Impact Eng 2007;34(10):1668–82.
[4] Langrand B, Deletombe E, Markiewicz E, Drazétic P. Riveted joint modeling for numerical analysis of airframe crashworthiness. Finite Elem Anal Des 2001;38(1):21–44.
[5] Ma Y, Lou M, Li Y, Lin Z. Effect of rivet and die on self-piercing rivetability of AA6061-t6 and mild steel CR4 of different gauges. J Mater Process Technol 2018;251:282–94.
[6] Sønstabø JK, Holmstrøm PH, Morin D, Langseth M. Macroscopic strength and failure properties of flow-drill screw connections. J Mater Process Technol 2015;222:1–12.
[7] Hoang N-H, Hanssen A-G, Langseth M, Porcaro R. Structural behaviour of aluminium self-piercing riveted joints: an experimental and numerical investigation. Int J Solids Struct 2012;49(23–24):3211–23.
[8] Hoang N-H, Porcaro R, Langseth M, Hanssen A-G. Self-piercing riveting connections using aluminium rivets. Int J Solids Struct 2010;47(3–4):427–39.
[9] Mucha J. The failure mechanics analysis of the solid self-piercing riveting joints. Eng Fail Anal 2015;47:77–88.
[10] Porcaro R, Langseth M, Hanssen A, Zhao H, Weyer S, Hooputra H. Crashworthiness of self-piercing riveted connections. Int J Impact Eng 2008;35(11):1251–66.

[11] Yan W, Xie Z, Yu C, Song L, He H. Experimental investigation and design method for the shear strength of self-piercing rivet connections in thin-walled steel structures. J Constr Steel Res 2017;133:231–40.
[12] Xie Z, Yan W, Yu C, Mu T, Song L. Tensile capacity of self-piercing rivet connections in thin-walled steel structures. J Constr Steel Res 2018;144:211–20.
[13] Han L, Chrysanthou A, Young K. Mechanical behaviour of self-piercing riveted multi-layer joints under different specimen configurations. Materials & Design 2007;28(7):2024–33.
[14] Ueda M, Miyake S, Hasegawa H, Hirano Y. Instantaneous mechanical fastening of quasi-isotropic CFRP laminates by a self-piercing rivet. Compos Struct 2012;94(11):3388–93.
[15] Kapidžić Z, Nilsson L, Ansell H. Finite element modeling of mechanically fastened composite-aluminum joints in aircraft structures. Compos Struct 2014;109:198–210.
[16] Hirsch F, Müller S, Machens M, Staschko R, Fuchs N, Kästner M. Simulation of self-piercing rivetting processes in fibre reinforced polymers: material modelling and parameter identification. J Mater Process Technol 2017;241:164–77.
[17] Dancette S, Fabregue D, Estevez R, Massardier V, Dupuy T, Bouzekri M. A finite element model for the prediction of advanced high strength steel spot welds fracture. Eng Fract Mech 2012;87:48–61.
[18] Combescure A, Delcroix F, Caplain L, Espanol S, Eliot P. A finite element to simulate the failure of weld points on impact. Int J Impact Eng 2003;28(7):783–802.
[19] Langrand B, Combescure A. Non-linear and failure behaviour of spotwelds: a “global” finite element and experiments in pure and mixed modes i/II. Int J Solids Struct 2004;41(24–25):6631–46.
[20] Hanssen A, Olovsson L, Porcaro R, Langseth M. A large-scale finite element point-connector model for self-piercing rivet connections. Eur J Mech A Solids 2010;29(4):484–95.
[21] Chtourou R, Leconte N, Chaari F, Haugou G, Markiewicz É, Zouari B. Macro-modeling of the strength and failure of multi-layer multi-steel grade spot welds: connector formulation, assembly model and identification procedure. Thin-Walled Structures 2017;113:228–39.
[22] Breda A, Coppieters S, Debruyne D. Equivalent modelling strategy for a clinched joint using a simple calibration method. Thin-Walled Structures 2017;113:1–12.
[23] Weyer S., Hooputra H., Zhou F.. Modeling of Self-Piercing Rivets Using Fasteners in Crash Analysis2006;:16.
[24] Bérot M, Malrieu J, Bay F. An innovative strategy to create equivalent elements for modelling assembly points in joined structures. International Journal for Computer-Aided Engineering and Software 2012;31(3):453–66.
[25] Chtourou R, Leconte N, Zouari B, Chaari F, Markiewicz E, Langrand B. Macro-modeling of spot weld strength and failure: formulation and identification procedure based on pure and mixed modes of loading. Eng Comput (Swansea) 2017;34(3):941–59.
[26] Sommer S, Maier J. Failure modeling of a self piercing riveted joint using LS-DYNA. 8th European LS-DYNA Users Conference, Strasbourg, France 2011:11.
[27] Wang C, Suo T, H-M.Gao PX. Determination of constitutive parameters for predicting dynamic behavior and failure of riveted joint: testing, modeling and validation. Int J Impact Eng 2019;132:103319.
[28] Palmonella M, Friswell MI, Mottershead JE, Lees AW. Finite element models of spot welds in structural dynamics: review and updating. Computers & Structures 2005;83(8–9):648–61.
[29] Xu S, Deng X. An evaluation of simplified finite element models for spot-welded joints. Finite Elem Anal Des 2004:20.
[30] Khandoker N, Takla M. Tensile strength and failure simulation of simplified spot weld models. Materials & Design (1980–2015) 2014;54:323–30.
[31] Bier M, Sommer S. Advanced investigations on a simplified modeling method of self-piercing riveted joints for crash simulation. 11th LS-DYNA Forum, Ulm, Germany 2012:9.
[32] Bier M, Sommer S. Simplified modeling of self-piercing riveted joints for crash simulations with a modified version of constrained interpolation spotweld. 9th European LS-DYNA Users Conference, Manchester, UK 2013:10.
[33] Dufour L, Bourel B, Lauro F, Haugou G, Leconte N. A viscoelastic-viscoplastic model with non associative plasticity for the modelling of bonded joints at high strain rates. Int J Adhes Adhes 2016;70:304–14.
[34] Schreier H, Orteu J-J, Sutton MA. Image correlation for shape, motion and deformation measurements. Boston, MA: Springer US; 2009.
[35] Abaqus Explicit 2018 Documentation - Dassault Systemes; 2018.
[36] Connector behavior - Massachusetts Institute of Technology, https://abaqus-docs.mit.edu/2017/English/SIMACAEELMRefMap/simaelm-c-connectorbehavior.htm; 2017.